ELSEVIER
Chemical Physics 251 (2000) 283–308
Chemical Physics
www.elsevier.nl/locate/chemphys

Coherent phonon spectroscopy of GaAs surfaces using time-resolved second-harmonic generation

Yu-Ming Chang [1], Li Xu, Harry W.K. Tom *

Dept. of Physics, University of California, Riverside 92521, USA

Received 14 June 1999

Abstract

The general theory and experimental considerations are presented for a novel all-optical time-domain technique for measuring low frequency vibrational modes of surfaces (phonons or adsorbate vibrational modes). A pump-laser pulse impulsively drives an initial displacement of the surface atoms. The subsequent free-induction decay of the coherent phonon modes of the surface atoms is detected by time-resolved second-harmonic generation (SHG). The spectral features are recovered by fitting the time-domain data to exponentially decaying sinusoids. This all-optical probe has advantages over inelastic particle scattering techniques because it can be applied at buried interfaces. It has signal to noise advantages over linear and spontaneous Raman techniques. This technique is demonstrated by measurement of surface optical phonon spectra on the clean GaAs (110)–relaxed–(1×1), GaAs (100)–(1×6), and GaAs (100)–(4×1) in UHV and of a local monolayer-scale interfacial mode at the buried native-oxide-covered GaAs (100). The chemical sensitivity is demonstrated by in situ oxidation of the GaAs (100)–(4×6). The general mechanism of generating coherent surface phonons is discussed in light of the symmetry selection rules. © 2000 Elsevier Science B.V. All rights reserved.

1. Introduction

Surface phonons, the atomic vibrational modes localized at surfaces [1], play a vital role in the dynamics of surface chemical reactions and in carrier-surface scattering. Substrate surface phonons are the modes by which most of the thermal energy is transferred between adsorbates and the substrate under normal reaction temperature conditions (300–1000 K). In contrast to surface acoustic modes, surface optical phonon modes have frequencies that are nearly resonant with adsorbate-substrate vibrational frequencies (5–10 THz). Moreover, surface optical phonons have electric dipole moments which allow them to couple efficiently to adsorbate charge-transfer states and internal vibrations as well as to charged particles (bulk carriers or incident particles). There has been considerable recent interest in the coupling of adsorbate vibrational modes to adsorbate-substrate vibrations [2], and to substrate bulk phonons and electronic states [3,4]. The participation of surface and interfacial optical phonon modes in vibrational relaxation and energy transfer and in surface-carrier scattering and trapping is relatively unexplored. In this paper, we discuss a novel time-domain optical technique to study surface phonon dynamics with femtosecond time resolution. We have demonstrated this technique on clean [5]

* Corresponding author.
[1] Present address: Dept. of Physics, National Dong Hwa University, Hualien, Taiwan, ROC.

0301-0104/00/$ - see front matter © 2000 Elsevier Science B.V. All rights reserved.
PII: S0301-0104(99)00306-7

and buried (oxide-covered) GaAs surfaces [6]. These studies open a new window to investigate the role of interface phonons in interface dynamics such as bulk-carrier-interface-phonon interaction, interface-carrier-interface-phonon interaction, non-equilibrium phonon populations, coherent control of interface phonons, and surface-phonon-induced surface chemical reactions.

There are various experimental tools for surface phonon studies. Inelastic particle-scattering techniques have the advantage of being wave-vector selective. High resolution electron energy loss spectroscopy (HREELS) [7,8] and helium atom scattering (HAS) [9,10] are well established techniques and surface phonon dispersion curves have been measured for a large number surfaces in pioneering work by H. Ibach and co-workers and J.P. Toennies and co-workers, respectively. HAS and HREELS in the impact regime have sub-monolayer sensitivity to surface adsorbates and to surface phonons but can only probe the vacuum/solid interface. In the long-range dipole interaction regime, HREELS has been used to observe Fuchs–Kliewer (F–K) phonons at clean [11,12] and buried semiconductor interfaces [13–16] and bulk-like modes [15] and standing wave modes [17] in thin film overlayers. While F–K phonons and thin film layer modes are confined to the interfacial region and may be sensitive to monolayer-scale interfacial properties through the induced interface current [15], the phonon displacements are dominated by bulk properties and are not 'localized' to the monolayer scale structure at the interface. In the long-range dipole interaction regime, HREELS loses its wave-vector selectivity. HREELS is particularly useful for detection of optical modes due to the charge of the electron probe. However, on semiconductor surfaces, the F–K mode dominates the response and it is difficult to observe high frequency local surface optical modes in the frequency range near the bulk LO phonon frequency. In HAS the probe is not charged and HAS is therefore uniquely sensitive to the acoustic modes. Most of the work using HAS has examined the frequency range of < 15 meV (< 3.5 THz).

Optical spectroscopies have the advantage that they can probe buried interfaces as well as UHV interfaces provided one side of the interface is transparent. However, they can only probe phonons in a narrow range of (wave-vector) q-space near the Γ-point ($q = 0$) of the surface Brillouin zone. This does not allow mapping of the full dispersion curve but the slope $\left.\frac{d\omega}{dq}\right|_{q=0}$ can be determined by optical grating techniques. The latter has been used for measurements of the speed of sound in thin films [18,19]. The optical phonon bands are relatively flat but such a measurement can at least determine if the Γ-point is a maximum or minimum energy point with respect to a given direction in the surface Brillouin zone and this information can be useful in comparing the experimentally found mode frequency with theory. Surface spontaneous Raman spectroscopy [20], IR absorption spectroscopy (IRAS) [21,22] and more recently visible-IR sum-frequency generation (SFG) [23,24] have been applied broadly to internal vibrational modes of adsorbates. Excluding hydrogen, only a handful of substrate–adsorbate vibration modes have been studied by Fourier Transform IRAS [25]. The low frequency modes (< 10 THz, 300 cm^{-1}, 40 meV) are difficult to observe because the surface Raman susceptibility is too low (without surface enhancement) to observe over the wings of the elastic peak and the source and detector combinations in the Far IR are not sensitive enough for submonolayer detection. Recently free electron Far IR sources have been used to obtain adsorbate–substrate vibrational spectroscopy [26]. New femtosecond-laser-based broadband terahertz radiation sources and time-domain detection [27,28] may be used in a more laboratory-scale environment for surface IR spectroscopy but no such studies have been reported to date. The only optical study of surface optical phonons that are localized on the monolayer scale has been reported for spontaneous Raman [29] and Resonance Raman Spectroscopy [30] of Sb monolayers on GaAs (110) in UHV. In general, linear and Raman optical techniques have shown little sensitivity to surface phonons because the bulk phonon response dominates the signal.

In the early 1990s, Kurz and co-workers [31,32] and Ippen and co-workers [33,34] demonstrated the excitation of coherent longitudinal optical (LO) phonons in *bulk* semiconductors, semimetals, and insulators using femtosecond laser pulses and their detection by time-resolved linear reflectivity. Our technique is based on those studies. The pump pulse

drives an initial displacement of the surface atoms that is time-coherent with respect to the arrival of the pump pulse. Because we are interested in the surface phonons, we detect the free-induction decay of the phonon modes by time-resolved second-harmonic generation (TRSHG). SHG has a well-established surface-to-bulk sensitivity for centrosymmetric media due to SHG being dipole-allowed at surfaces but dipole-forbidden in the bulk [35]. As pointed out by Shen and co-workers [36], even on non-centrosymmetric media such as GaAs, there is substantial surface sensitivity due either to the SH susceptibility of the surface electronic structure or the ability to exploit particularly favorable tensor properties of the SH susceptibility tensor to suppress the contribution of the bulk.

The period corresponding to 10 THz is 100 fs so the probe-laser pulse must be shorter than 100 fs to efficiently detect phonon oscillations of frequency up to 10 THz in the time domain. In this work we used 35 fs pump pulses to drive and detect phonons in the 3–10 THz range on GaAs surfaces and used various probe-SH polarization combinations and crystal orientations. We chose GaAs because bulk LO phonons had been coherently excited by femtosecond laser pulses and probed by time-resolved linear reflection by Kurz and co-workers [31,32]. The well-known bulk LO phonon feature at 8.8 THz could be used as a relative amplitude standard for our surface phonon sensitivity. The bulk LO phonon frequency, lifetime, and dephasing time have been measured as a function of temperature and carrier density in earlier studies [37–40].

We will first present the basic experimental and theoretical details of the measurement. Then we will present the first localized surface optical phonon spectra for the native oxide-covered GaAs surface [6] as well as the clean and reconstructed GaAs (110)–relaxed–(1×1) [5], GaAs (100)–(1×6) and GaAs (100)–(4×1) surfaces. The spectra are unique in that they first can be sensitive to motion parallel to the surface and secondly are detected in the frequency region near the bulk LO phonon that is largely obscured in similar HREELS measurements by the F–K mode. While the GaAs (110)–relaxed–(1×1) has been studied by both HAS and HREELS before, no spectra for the other surface systems have been reported. In comparison to the previous Raman spectroscopy observation of a mode buried under 1–2 monolayers of Sb on GaAs, our monolayer-scale interface mode is buried under the 50–80 Å thick native oxide and demonstrates that the technique can be used in commercially-relevant semiconductor-oxide interface geometries. We also present phonon spectral changes during in situ oxidation of GaAs (100)–(4×6). This study establishes the chemical sensitivity of the technique and in conjunction with the other surface phonon spectra gives us some insight into the native-oxide-GaAs (100)-interface phonon. We will then discuss what these studies tell us about the general applicability of this new probe, including the driving mechanism, the relative size of the surface signal compared to the bulk, the relative merits compared to HREELS, and future possibilities using this technique.

2. Theory of TRSHG phonon spectroscopy

Our new coherent surface optical phonon spectroscopy [5,6] is based on impulse stimulation of the phonons with a pump pulse and then detection of the free-induction decay of the phonon modes by time-resolved second-harmonic generation. We will first discuss the possible driving mechanisms and then the detection scheme.

Let us denote the amplitude of the n-th phonon mode with wave-vector $\boldsymbol{q}$, by $Q_{n,\boldsymbol{q}}$. In the harmonic approximation, each of the phonon modes obeys:

$$\ddot{Q}_{n,\boldsymbol{q}} + (2/T_n)\dot{Q}_{n,\boldsymbol{q}} + \omega_n^2 Q_{n,\boldsymbol{q}} = F_{n,\boldsymbol{q}}(t)/\mu_n\,, \qquad (1)$$

where T_n, ω_n, $F_{n,\boldsymbol{q}}$ and μ_n are the n-th mode's dephasing time, resonant angular frequency, external force, and effective mass, respectively. In Eq. (1), we have suppressed the index $\boldsymbol{q}$ for the dephasing time, frequency, and effective mass for reasons that will become apparent. The dispersion of an optical phonon mode, $\partial\omega/\partial\boldsymbol{q}$, will be less than 5 THz Å. We apply the force with a pump-laser pulse which has a lateral dimension given by the beam size and angle of incidence of the laser. For example, in this experiment we used a pump pulse with a Gaussian spatial profile with waist $\omega_0 \sim 10$ μm, i.e., $I(r) \propto \exp(-2r^2/\omega_0^2)$. By Fourier transform, $I(\boldsymbol{q}_{\parallel}) \propto \exp(-\boldsymbol{q}_1^2\omega_0^2/8)$ and the pump-beam-induced force

can only have substantial contribution from $q_{\parallel} < (2\sqrt{2}/\omega_0) \sim 3 \times 10^{-5}$ Å^{-1}. For such a small range of $q_{\parallel}$, dispersion will cause no more than a 1.5×10^{-4} THz inhomogeneous frequency broadening which is negligible compared to the phonon dephasing rate which is typically > 0.1 THz. We also do not expect dispersion in the dephasing rate or effective mass of the mode to be important over this small range of wave-vectors.

The average motion of the atoms within the pump/probe beam area will be the band-integrated displacements of the n modes, $Q_n(t)$, where the integration is again over the same spatial components roughly $q_{\parallel} \leq \sim 3 \times 10^{-5}$ Å^{-1}. In thermal equilibrium the amplitude of each $Q_{n,q}$ is given by Bose–Einstein statistics. Because there is no spatial coherence between the modes of different q, the band-integrated displacement for each mode branch n will be washed out spatially over the probe beam. Because there is no temporal correlation with the arrival of the pump pulse, any small displacement on a given laser-probe pulse will be averaged to zero over the many pump–probe events that are averaged in a given experiment. However, each of the $q_{\parallel}$ components of the force applied by the pump-laser pulse is temporally and spatially in phase so all the $q_{\parallel}$ modes of the same branch n will oscillate in phase. By coherently adding the displacements of each $q_{\parallel}$ mode, the motion behaves as if all energy were in a single $q_{\parallel} = 0$ mode with an extremely non-thermal Bose–Einstein occupation number.

The phonon motion will follow the driving force as in Eq. (1) and the formal solution can be easily derived:

$$Q_n(t) = \frac{1}{\mu_n \varpi_n} \int_{-\infty}^{t} \mathrm{d}t' F_n(t') \mathrm{e}^{-(t-t')/T_n} \times \sin\big(\varpi_n(t-t')\big), \tag{2}$$

where $\varpi_n = \sqrt{\omega_n^2 - 1/T_n^2}$. In order to use this as a spectroscopic tool, we want to observe the free-induction decay of the modes to determine the natural frequencies and dephasing times of the modes. This requires that the force not only turn on rapidly compared to the phonon period and dephasing time in order to drive a large initial displacement but also turn off quickly to allow free oscillation. Once the force is turned off, the phonon amplitude follows free induction decay and

$$Q_n(t) \propto A_n \sin(\varpi_n t - \varphi_n) \mathrm{e}^{-t/T_n}, \tag{3}$$

where the q-integrated initial amplitude of the n-th mode is A_n and the initial temporal phase of the mode is φ_n. The initial phase is given by:

$$\tan\varphi_n = \frac{\int_{-\infty}^{\infty} \mathrm{d}t'(t') \mathrm{e}^{t'/T_n} \sin\varpi_n t'}{\int_{-\infty}^{\infty} \mathrm{d}t' F_n(t') \mathrm{e}^{t'/T_n} \cos\varpi_n t'}. \tag{4}$$

Examination of Eq. (4) shows that if the time duration of the force is much shorter than the phonon period or dephasing time and applied at $t = t_F$ then $\varphi_n = \varpi_n t_F$. The absolute value of A_n may or may not be larger than the root-mean-squared amplitude of the n-th mode ($\propto \sqrt{k_B T}$). However, because this motion is time-coherent with the arrival of the pump, it can be detected by signal averaging over many pump pulses. The formalism above applies even if the modes are critically damped or overdamped. However, in this paper, we only detected underdamped modes and the mode frequencies we cite are $\bar{\nu}_n = \sqrt{\nu_n^2 - (2\pi T_n)^{-1}} \sim \nu_n$.

We now turn to the laser-induced driving mechanisms suitable for coherent phonon spectroscopy. There are four general mechanisms. The first three were developed to explain ultrashort-laser-pulsed excitation of coherent optical phonon oscillations in bulk materials. In order for the TRSHG technique to apply at least one or more of these four mechanisms must apply to the interfacial system of interest.

In the first two mechanisms, the pump pulse rapidly increases the carrier density leaving the atoms suddenly in vibrationally excited positions with respect to the new equilibrium positions of the atoms. Ippen and co-workers coined the phrase Displacive Excitation of Coherent Phonons (DECP) [33,34] to describe when the carrier density suddenly changes the dielectric screening of the atomic bonding potentials. The laser pulse must inject carriers with a

sufficiently rapid rising edge so the atoms cannot follow the changing potential adiabatically. This change is equivalent to changing the equilibrium lattice constant so only fully symmetric A' or A_1 modes can be excited. A second mechanism applies for semiconductors or interfaces with a built-in surface electric field that induces static lattice displacement by the piezoelectric effect. When the injected carriers rapidly screen the field, the lattice is suddenly free to oscillate about the field free (or lower field) lattice equilibrium positions. Here, the pump-laser pulse must be short enough for the injected carriers to screen the field on a shorter time scale compared to the phonon period. Kurz and co-workers have shown this is the dominant mechanism for exciting the bulk LO phonons in the depletion region of GaAs with femtosecond laser pulses [31,32]. One might expect this mechanism to be particularly useful for studying buried semiconductor interfaces under voltage-biased conditions.

For both DECP and field-screening mechanisms, the time scale of the force can be made shorter than the laser-pulse duration by increasing the pump-pulse intensity. Ippen and Kurz pointed out that a signature of DECP and field-screening mechanisms should be that the coherent phonon amplitude is sine- and cosine-like with respect to the arrival of the pump, respectively, because the initial displacements are either zero or a maximum, respectively. Since the effective 'start-time' of the force depends on the carrier dynamics and pump intensity, the initial phase of the phonon is somewhat problematic to characterize as sine- or cosine-like with respect to the arrival time of the pump pulse. A signature of both mechanisms is that the initial phase of oscillation should shift to earlier time with increased pump intensity. Another signature is that the coherent phonon motion is independent of the polarization of the pump pulse or the orientation of the sample with respect to the plane of incidence of the pump pulse. Both mechanisms apply when the coherence time of the laser-injected carriers is much shorter than the lifetime of the initial electronic excitation. In that case we can neglect electron-phonon coupling during the coherence time and consider the electronic excitation to be instantaneously in local equilibrium (all states of equivalent energy are equally likely) so there is no memory of the laser polarization or phase.

In contrast, the remaining two mechanisms depend on both the crystal orientation and the pump polarization. The third driving mechanism is stimulated Raman excitation (SRE). The force $F_n = \frac{1}{2}\varepsilon_0 Re\left[\left.\frac{\partial\alpha_{ij}^{(1)}}{\partial\hat{Q}_n}\right|_0 E_i E_j^*\right]$, where $\hat{Q}_n$ is the lattice displacement vector of the n-th mode, $\overleftrightarrow{\alpha}^{(1)}$ is the linear optical polarizability tensor per unit cell, and E is the laser electric field. The differential linear polarizability per unit cell is evaluated at the equilibrium point $Q_n = 0$ and is the Raman susceptibility tensor. The Raman scattering cross-section is proportional to the square of the Raman susceptibility tensor. This mechanism dominates coherent vibrational excitation of molecules and molecular crystals [41]. This effect was exploited earlier by Bron and co-workers to drive coherent LO phonons in bulk solids with picosecond pulses in coherent anti-Stokes Raman spectroscopy studies [42]. Because SRE is a coherent process, the phase of the n-th phonon at angular frequency $\omega_n = \omega_1 - \omega_2$ is controlled by the phase of the laser fields $E(\omega_1)$ and $E^*(\omega_2)$. For excitation with a single femtosecond laser pulse, the full laser bandwidth must be considered so $F_n(t)$ is simply proportional to the laser intensity $I(t)$. The sign of the force is determined by the Raman susceptibility and the relative phase difference between E_i and E_j. The fourth driving mechanism is vibrational excitation through electronic excitation and rapid de-excitation, i.e., the Franck–Condon effect for molecules or the generalized Menzel–Gomer–Redhead (MGR) type mechanism for surfaces [43–45]. The atoms accelerate while briefly in the electronically excited state and are vibrationally excited when the system returns to the ground electronic state.

Both SRE and MGR have Raman selection rules and the time scale of the applied force does not depend on pump intensity. In SRE, the pump laser induces a coherence between the ground and excited state and the force is only applied during the pump-laser pulse. In MGR, the pump laser induces a transient population in the excited state. The time duration of the force will follow the excited state population. In the linear regime (small peak population), this will be simply $F(t) \propto \mathrm{e}^{-t/\tau}\int_{-\infty}^{t} I(t')\mathrm{e}^{t'/\tau}\mathrm{d}t'$ where τ is the excited state population lifetime. Since the laser-matter interaction always

involves induced coherence and population the dominance of SRE or MGR depends on the resonance conditions, lifetime, and dephasing time of the excited state. If the pump laser induces the initial electronic excitation by direct photoexcitation and the de-excitation returns the system to the initial ground state then the phonon mode that is excited will follow Raman symmetry rules with respect to the pump laser field polarization.

More generally, however, MGR can be driven by secondary electronic excitations of the surface states induced by other pump-laser-induced surface or bulk electronic excitations. Recently, for example, ultrafast desorption of adsorbates under femtosecond laser irradiation has been attributed to multiple MGR excitations involving the hot substrate-electron population [46–48]. Both DIET (desorption induced by electronic transitions) and DIMET (desorption induced by multiple electronic transitions) [49] invoke MGR-like coupling to transfer energy from the substrate electrons to the adsorbate center-of-mass motion. Similarly, carriers driven to interfaces by the depletion fields in semiconductors can induce interface-state excitations. In these secondary electronic excitations, the memory of the laser polarization is lost and any mode that is Raman active can be excited. In this article, we will assume that we can neglect these secondary excitations for the purpose of driving coherent optical phonon oscillations. The surface or bulk electronic states that make the secondary excitations have lifetimes that are longer than half the phonon period (> 50 fs) so the phonons that are excited in individual MGR events will not add constructively and will therefore not be detectable as coherent phonon oscillations.

We will therefore assume that if the mode amplitudes depend on the polarization of the pump then the first two mechanisms (DECP and field screening) can be ruled out and that the mode must be driven by SRE or MGR. Under those conditions, Raman polarization-selection rules must apply and therefore, we can determine the symmetry of the phonon mode by examining the amplitudes under various combinations of laser polarization and crystal orientation.

In Tables 1 and 2, we show the character table, IR activity, and linear, Raman, and hyper-Raman susceptibility-tensor elements associated with each mode symmetry for the point groups m and $mm2$. These are the point groups of the GaAs (110) and (100) surfaces, respectively. We see by the Raman tensor elements, R_{ijk}, for example, that on the (110) surface, where $x=[001]$, $y=[1\bar{1}0]$, and $z=[110]$, that the only elements that can excite the A'' mode are R_{xyy} and R_{zyy}. The convention used here is $R_{ijk} = \partial\alpha_{ij}^{(1)}/\partial Q_k$ so the first 2 indices correspond to the directions of the applied optical fields. The first two indices may be permuted and are not listed separately in the table. To excite the A'' mode, the pump fields have to be applied to either x and y or z and y. The latter can be accomplished with a single pump pulse if the $y=[1\bar{1}0]$ is oriented in the plane of incidence and the pump polarization is p-polarized (E along both y and z). In Table 3, we show the symmetry of the modes that can be excited by the SRE and (photoexcited) MGR mechanisms for various crystalline axes in the plane of incidence and pump polarizations. The principal crystalline axes for the [100] surface are $x=[011]$, $y=[0\bar{1}1]$ and $z=[100]$.

Together the four mechanisms seem applicable to a wide range of interface systems. Particularly in the case of SRE and MGR, the driving force can be resonantly enhanced by tuning the laser frequency to an electronic state-transition frequency. However, the electron-phonon coupling still must be large enough to produce a detectable coherent phonon oscillation. The spontaneous Raman scattering cross-section (proportional to the squared amplitude of the Raman susceptibility tensor elements) is tabulated for many molecules and crystalline solids. The electron-phonon coupling per unit volume in bulk solids is much weaker than in molecules due to the

Table 1
Character tables and associated IR activity, and linear and nonlinear susceptibility tensor elements for the point group m

m	E	σ_{xz}	IR	α_{ij}	R_{ijk}	β_{ijkl}
A'	1	1	T_x, T_z, R_y	*xx, yy, zz, xz*	*xxx, yyx, zzx, xzx, xxz, yyz, zzz, xzz*	*xxxx, xxzx, zzxx, yyxx, yyzx, zzzz, xxzz, zzxz, yyxz, yyzz*
A''	1	-1	T_y, R_x, R_z	*xy, zy*	*xyy, zyy*	*xyzy, yzzy, yxxy, yyyy*

Table 2
Character tables and associated IR activity, and linear and nonlinear susceptibility tensor elements for the point group *mm2*

mm2	E	C_2	σ_{xz}	σ_{yz}	IR	α_{ij}	R_{ijk}	β_{ijkl}
A_1	1	1	1	1	T_z	*xx, yy, zz*	*xxz, yyz, zzz*	*zzzz, zxxz, zyyz*
A_2	1	1	−1	−1	R_z	*xy*	–	–
B_1	1	−1	1	−1	T_x; R_y	*zx*	*zxx*	*xxxx, xyyx, xzzx*
B_2	1	−1	−1	1	T_y; R_x	*zy*	*zyy*	*yyyy, yxxy, yzzy*

3-dimensional delocalization of both the electronic and vibrational excitation modes. For surfaces (2 dimensions), on the other hand, the electron-phonon interaction can be intermediate between that for a molecule and a 3-dimensional solid. Lateral surface reconstruction and the 5–10% vertical displacement of the topmost 1–3 atomic layers of most clean surfaces in ultrahigh vacuum are clearly driven by the relative strength of the electron-phonon coupling at surfaces compared to bulk solids. We expect that the Raman susceptibility per atomic layer of a reconstructed surface should be larger than in the corresponding bulk.

We now turn to our detection scheme. We use the coherent time-domain analog of stimulated hyper-Raman spectroscopy. We detect the interfacial coherent lattice motion using the differential second-order optical susceptibility tensor, $\partial\overleftrightarrow{\chi}^{(2)}(2\omega)/\partial\hat{Q}$. The SH electric field is driven by the nonlinear polarization $P_i(2\omega)$ at the surface. The SH susceptibility tensor may be expanded to first order in the phonon displacement:

$$P_{\mathrm{i}}(2\omega) = \left[\chi^{(2)}_{ijk}(2\omega) + \sum_{n,\boldsymbol{q}}\left(\partial\chi^{(2)}_{ijk}(2\omega)/\partial\hat{Q}_{n,\boldsymbol{q}}\right)_0 Q_{n,\boldsymbol{q}}\right] \times E_j(\omega)E_k(\omega). \tag{5}$$

The subscripts i, j, k are the indices of the usual vector projections and the differential second-order polarizability is evaluated at the equilibrium point ($Q=0$). Only the $\boldsymbol{q}$-integrated displacement $Q_n(t)$ will be detectable in this pump–probe experiment as a function of pump–probe-time delay. The SH intensity is proportional to $|P|^2$. Experimentally the oscillatory part of the total SH is small so we ignore terms of order A_n^2. After the driving force is 'off', we expect to fit the oscillatory part of the SH intensity to the form:

$$S(t) \propto \sum_n S_n \sin(\omega_n t - \varphi_n)\mathrm{e}^{-t/T_n}, \tag{6}$$

where S_n is a real number and will depend on the initial coherent phonon amplitude A_n and on the detection geometry through the background SH susceptibility $\chi^{(2)}_{ijk}$ and hyper-Raman tensor elements $\partial\chi^{(2)}_{ijk}(2\omega)/\partial\hat{Q}_n$.

In Table 4, we list the symmetry of the modes that can be detected by the SH probe through the hyper-Raman tensor. The convention used here is $\beta_{ijkl} = \partial\chi^{(2)}_{ijk}/\partial\hat{Q}_l$. All elements generated by permutations of the first 3 indices have the same symmetry but have not been listed separately.

In general, the TRSHG surface phonon measurement will have additional pump–probe time-dependent background due to phonons in the near surface bulk and carrier dynamics in the surface and near surface bulk. The full expression for the time-depen-

Table 3
Mode symmetry (Raman) selection rules for coherent excitation by SRE or MGR mechanisms on GaAs (110) and (001) surfaces

Pump polarization	GaAs (110) *m*		GaAs (100) *mm2*	
Axis in incident plane	$x=[001]$	$y=[1\bar{1}0]$	$x=[011]$	$y=[0\bar{1}1]$
p	A'	$A'+A''$	A_1+B_1	A_1+B_2
s	A'	A'	A_1	A_1

Table 4
Mode symmetry (hyper-Raman) selection rules for detection of coherent motion by time-resolved SHG on GaAs (001) and (110) surfaces

SH probe geometry	GaAs(110) m		GaAs(100) $mm2$	
Axis in incident plane	$x=[001]$	$y=[1\bar{1}0]$	$x=[011]$	$y=[0\bar{1}1]$
p_{in}–p_{out}	A'	$A'+A''$	A_1+B_1	A_1+B_2
p_{in}–s_{out}	A''	A'	B_2	B_1
s_{in}–p_{out}	A'	$A'+A''$	A_1+B_1	A_1+B_2
s_{in}–s_{out}	A''	A'	B_2	B_1

dent SH polarization in reflection from the surface must include:

$$\frac{P_i(2\omega,t)}{E_j(z=0)E_k(z=0)} \propto \left[\chi^{(2)}_{ijk}(2\omega) + \sum_n \left.\frac{\partial\chi^{(2)}_{ijk}(2\omega)}{\partial\hat{Q}_{n,\boldsymbol{q}=0}}\right|_0 Q^S_n(t) + \frac{\partial\chi^{(2)}_{ijk}(2\omega)}{\partial n_e}n_e(t) + \frac{\partial\chi^{(2)}_{ijk}(2\omega)}{\partial n_{\mathrm{h}}}n_{\mathrm{h}}(t)\right]_{\mathrm{S}} + \int_0^\infty\left\{\mathrm{d}z\,\mathrm{e}^{i(k_z(2\omega)+2k_z(\omega))z}\left[\chi^{(2)}_{ijk}(2\omega,z) + \sum_n \left.\frac{\partial\chi^{(2)}_{ijk}(2\omega)}{\partial\hat{Q}_{n,\boldsymbol{q}=0}}\right|_0 Q^B_n(z,t) + \frac{\partial\chi^{(2)}_{ijk}(2\omega)}{\partial n_e} \times n_e(z,t) + \frac{\partial\chi^{(2)}_{ijk}(2\omega)}{\partial n_{\mathrm{h}}}n_{\mathrm{h}}(z,t) + \chi^{(3)}_{ijkl}E_{\mathrm{DC},l}(z,t)\right]_{\mathrm{B}}\right\}, \quad (7)$$

where the first set of terms enclosed in square brackets is the surface SH susceptibility (subscript S) which changes due to pump-induced surface phonons, electrons, and holes, respectively, while the second set of terms enclosed in square brackets is the bulk SH susceptibility (subscript B) which changes due to bulk phonons, electrons, holes, and the DC electric field (E_{DC}), respectively. The DC electric field is due to the static arrangement of carriers and can change in time as the injected carriers diffuse and recombine in the near surface region. The bulk susceptibility is integrated over the bulk media from $z=0$ to ∞ with the phase-matching factor $\exp[i(k_z(2\omega)+2k_z(\omega))_z]$. This integral is the spatial Laplace transform of the bulk susceptibility. In centrosymmetric media, the bulk dipole-allowed SH susceptibility is zero and the surface and bulk quadrupole-allowed SH susceptibility contribute. In Si, the bulk quadrupole-allowed susceptibility generates an SH field that is comparable to that from the Si/SiO_2 interface [50]. In non-centrosymmetric bulk materials like GaAs, there is a non-zero dipole-allowed SH susceptibility. In the depletion region of a semiconductor there can be significant contribution from the depletion field and inhomogenous carrier distribution. The relative contributions from the depletion field (electric field-induced SHG term) in comparison to the bulk was studied for the native-oxide-covered GaAs (100) [51] and the enhanced contribution of the surface electronic states on clean $c(4\times4)$ and (2×4) reconstructed surfaces of GaAs (100) has also been reported [52]. In thin film geometries, the spatial dependence of the carriers, phonon amplitude, and electric field can be complicated so the spatial integral is important.

In transient cases, the bulk SH signal can change due to carrier relaxation in time or carrier diffusion in space. In our experiments, we used 850 and 425 nm radiation as the fundamental and second-harmonic respectively on GaAs. The dielectric constants at these wavelengths in GaAs make the SH in these experiments sensitive to the topmost 150 Å. This short distance is about half determined by the optical attenuation of 425 nm light in the bulk. In this paper we will not discuss the carrier dynamics in the

transient bulk signal. In comparison to time-resolved linear reflectivity, time-resolved SHG is more sensitive to the carriers closest to the surface where the most interesting depletion-field physics occurs. A study of the surface trapping dynamics and carrier dynamics in the depletion region using the transient bulk SH signal will be published separately.

Terms like $\partial\chi^{(2)}_{ijk}/\partial n_e$ suggest that the hyper-Raman selection rules for phonons might not apply if the phonon displacement can also drive a carrier oscillation $n_e(t)$. However, the SH would be modulated by the product $(\partial\chi^{(2)}_{ijk}/\partial n_e)(\partial n_e/\partial\hat{Q}_l)$ which has the same symmetry as the hyper-Raman tensor. Similarly, the optical phonon could induce an electric field. However, the electric-field-induced SH also has hyper-Raman selection rules. Thus the hyper-Raman selection rule applies rigorously in detection of phonons by TRSHG.

We note that the hyper-Raman and Raman selection rules that we apply follow the symmetry of the underlying substrate. On a reconstructed surface, the overlayer structure can have a different symmetry from the substrate and if the laser beam only sampled one domain of this surface one would see a different symmetry. However, because of steps and other pinning defects, there are many domains and over a sample size as large as the laser beam (several μm^2) there are equal numbers of domains in the different orientations allowed by the bulk symmetry. Thus, a mode that is observed in TRSHG to have only a z-dipole moment normal to the surface may also have an in-plane dipole moment in a single unit cell of the reconstructed overlayer but this motion is not detected because of the same in-plane motion in anti-phased domains. For the reconstructions of GaAs in this paper the overlayer symmetry is always that of the substrate.

3. Experimental setup and sample preparation

The experiments were carried out either in air or under ultrahigh vacuum conditions (base pressure $< 2 \times 10^{-10}$ Torr). Both GaAs (110) and (100) were highly n-doped (3×10^{18} Si/cm^3) and the depletion field was calculated to be 740 kV/cm over the topmost 140 Å. The native-oxide-covered surface was cleaned with solvents ending in methanol. The clean GaAs surfaces were prepared in UHV by sequential Ar^+-ion sputtering and annealing cycles. The native oxide was removed in situ by cycles of sputtering at 500 eV at an ion current sufficient to remove 2–3 monolayers assuming yield of 1 atom per ion and of thermal annealing at 540°C for 20–30 min thermal annealing. Cycles were continued until the bulk LEED pattern was observed and the oxygen Auger electron spectroscopy peak was $< 1\%$ of the Ga Auger peak. The various reconstructions were obtained with a short 500 eV sputter sufficient to remove 0.25 monolayers assuming yield of 1 atom per ion and then 15–20 min of thermal annealing at various temperatures. The (1×1)–relaxed reconstruction of GaAs (110) was prepared with 550°C annealing cycles until a sharp LEED pattern appeared. The SH intensity reached a maximum for the best prepared surfaces and was very sensitive to adsorbates so we used the SH intensity as a monitor of surface quality. Subtle changes in the surface structure that could not be detected by LEED were detectable by SH. On the (100) surface, there is a rich literature of the many reconstructions that can be generated by either MBE deposition and annealing, sequential ion bombardment and annealing, or simultaneous ion bombardment and annealing. We studied the (1×6), (4×6) Ga-rich, and (4×1) Ga-rich reconstructions and found that the annealing temperatures agreed with the nominal temperatures and in increasing temperature order as in the literature [53]. We used the LEED patterns to orient the samples with respect to the optical plane of incidence.

The optical experiments were performed using 850 nm, 35 fs laser pulses from a Ti:Sapphire Kerr–Lens Modelocked laser oscillator with an ~ 80 MHz repetition rate. The weak probe beam was derived from the pump beam with a beam splitter and the pump beam was passed through a delay line. Pump and probe pulses overlapped spatially in a Gaussian spot with 10 μm waist on the sample surface at $\sim 45°$ angle of incidence with a $\sim 3°$ angular separation in the plane perpendicular to the plane of incidence to separate the beams. The second-harmonic generation of the probe beam was detected as a function of time-delay between pump and probe. The SH reported throughout this article was detected

in p-in and p-out geometry. There is of course no general requirement to do so. The SH was separated from the fundamental with color and interference filters and detected with a low noise photomultiplier tube (PMT) cooled to 0°C. The pump-induced change in the probe SH was obtained by processing the PMT output with a lockin amplifier synchronized to the mechanical chopping rate of the pump beam. The typical SH signal from the bulk GaAs was 5×10^7 SH photons/sec for 20 mW average power in the probe fundamental beam. We detected SH photons with approximately 7% efficiency yielding a background signal of order 3.5×10^6 count/s. The SH oscillation peak for the bulk LO phonon (see Fig. 1 10% of transient ΔSH) was about 1% of the background or 3.5×10^4 count/s. The dark count for the cooled PMT was 1 count/s so the dominant noise was due to the laser amplitude fluctuations, the SH photo-count shot noise, and laboratory electronic background noise. If we were shot noise limited alone, we would expect SH background fluctuations of $\sqrt{3.5 \times 10^6} = 1.9 \times 10^3$ counts to be detected over 1 s of averaging time on the lockin and the signal to noise ratio to be ~ 19. Improvements scale as the square root of the averaging time so we would require a 60 s averaging time per time-delay point to get a S/N of ~ 150 with respect to the peak phonon amplitude. In the work presented here, we obtained S/N of ~ 50 ($3\times$ more noise than shot-noise limit)

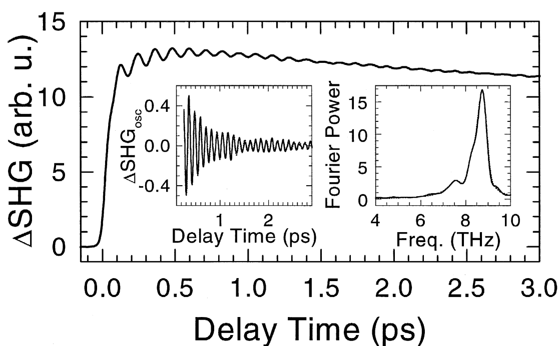

Fig. 1. TRSHG signal for native-oxide-covered GaAs (100). The injected carrier density was $7.2 \times 10^{17}/\mathrm{cm}^3$. Left and right insets show the oscillatory part of the time domain data and the Fourier power spectrum of the oscillatory part. Data (solid) and fit (dashed).

in our longest scans in which we rapidly scanned 512 time-delay points and averaged hundreds of scans over ~ 8 hours. Fortunately for these studies, clean GaAs is not reactive to molecular gases in the UHV chamber with the ion gauge filament off so the clean samples could be maintained for long periods of time. While the phonon spectra were sensitive to the details of sample preparation, the main features of the spectra reported here were reproduced in several measurements and the long-time-scan data sets were consistent with the short-time-scan data sets accumulated during the long-time scan.

4. Experimental results and data analysis

Because the most unique advantage of the TRSHG phonon spectroscopy technique is the ability to use it at buried interfaces, we begin with a measurement of a localized phonon mode at the native-oxide-covered GaAs (100) [6]. In Fig. 1 we show the typical TRSHG data set. Here we performed the measurement on the native-oxide-covered GaAs (100) surface held in air. The pump-induced change in reflected SHG is shown as a function of pump–probe time delay. We see a rapid change near zero time delay due to carrier injection ($\partial\chi^{(2)}_{ijk}/\partial n_{e,h}$) and rapid carrier-induced screening of the depletion field ($\chi^{(3)}_{ijkl}E_l$) in the bulk. A slow decay follows due to carrier recombination and diffusion dynamics in the bulk as well. Ultrafast carrier dynamics in the depletion region is well studied and is known to drive coherent LO phonon oscillations in the bulk [31]. We focus presently on the small rapid oscillation on this background signal (see left inset). The oscillatory part, $S(t)$, was assumed to be in free-induction decay after the first 150–200 fs of delay time and we removed the remaining time-dependent background by Fourier filtering frequencies < 3 THz. The oscillation amplitude was $\sim 10\%$ of the pump-induced TRSHG signal and $\sim 1\%$ of the total probe SHG intensity. Because this data was obtained over many scans, it is clear that the oscillation was coherent with the arrival of the pump pulse and due to excitation of coherent phonons. In the right inset of Fig. 1, we show the apodized Fourier power spectrum of $S(t)$ (square of the apodized Fourier transform of

$S(t)$). The Fourier transform of $S(t)$ on a semi-infinite time interval is the sum of complex Lorentzians,

$$F[(S,t)] \propto \sum_n S_n e^{-i\varphi_n}(\omega - \omega_n - i\Gamma_n)^{-1}, \qquad (8)$$

however, the Fourier transform over the finite time interval of the time-domain data will have spectral artifacts (side lobes). To suppress those artifacts we used an apodized Fourier transform:

$$F(\omega) = \int_{t_1}^{t_2} S(t)\, g(t) e^{i\omega t} dt, \qquad (9)$$

where the endpoints of the time-domain data are t_1 and t_2, and the apodizing function was $g(t) = \cos(\pi/2 \cdot (t-t_1)/(t_2-t_1))$. The apodizing function is a maximum at the beginning of the time interval when the oscillation is a maximum and is zero at the end of the time interval when the oscillation has decayed. While the apodization effects the apparent frequency resolution in the power spectra shown in the figures, it does not effect the fits. When we fit the data in the frequency domain we always compared the apodized Fourier transforms of the time-domain data and of the fit function over the same time interval. The agreement between the dashed and solid lines in the time domain assures us that we have fit the data correctly.

It is important to point out the difference between coherent spectra and conventional linear optical spectra. In incoherent linear reflectivity or transmission, a narrow spectral feature shows as a loss of reflected/transmitted intensity from the background and is proportional to the imaginary part of the complex Lorentzian susceptibility of the oscillator, $Im[1/(\omega - \omega_0 + i\Gamma)] = -\Gamma/((\omega - \omega_0)^2 + \Gamma^2)$. For oscillators that are coupled to complex electronic systems (Fermi resonances, for example), an arbitrary phase of the complex Lorentzian susceptibility adds to the background and the resulting line-shapes are called Fano line-shapes. In time-domain spectroscopy, one measures the oscillation as a function of the pump–probe time delay and the initial phase of each mode oscillation is set by the driving force and mechanism that may be different for each mode. As shown in Eq. (3), even if the driving force is a symmetric function such as a Gaussian during the pump pulse, the initial phase of the oscillator will depend on the time duration of the laser pulse in comparison to the dephasing time and period of the oscillator. Only in the limit of an infinitely short driving force will the phonon motion be pure cosine- or sine-like. Thus, the real and imaginary parts of the $F[S(t)]$ have no a priori relation to the real and imaginary part of the Lorentzian frequency response. As a result it only makes sense to plot the Fourier power spectrum. But since each mode can have a different initial phase, it is not easy 'by inspection' to see the spectral features in the frequency domain especially when the modes overlap. In Fig. 1 (right inset) it is tempting to just pick the 3 frequencies with the maximum peak heights as the center frequencies of three modes. Instead we rely on our nonlinear curve fitting routine to find the spectral parameters. Although there are a lot of fit parameters (the initial phase is now an additional factor compared to incoherent spectroscopy), the time-domain data is sufficiently rich in detail. In practice the nonlinear fit converges with reasonable confidence by iteratively fitting A_n and φ_n to minimize the chi-square of the time-domain data and ν_n and T_n to minimize the chi-square of the frequency domain-derived data. The apodized Fourier transform is needed to prevent the fit routine from fitting side-lobe artifacts in the frequency domain.

When there are many overlapping peaks we can further constrain the fits by simultaneously fitting phonon spectra taken with different excitation geometries. In that case, all spectra are fit with the same ν_n and T_n however each spectrum has a different linear combination of modes and therefore must be fit with different A_n and φ_n. We did this in the data presented in Figs. 4 and 5. In principle, one could further constrain the data fits by assuming that the driving mechanism for a given mode is the same in all geometries. Then the initial phase φ_n is independent of the geometry as well and only the mode amplitudes (with sign) differ between the various measurement geometries. Furthermore, if one assumed the specific driving mechanism, for example SRE, then one could use Eq. (4) and the temporal profile of $F(t)$ to eliminate φ_n as an independent parameter altogether. In these experiments, we did not know the driving mechanism beforehand and since two or more mechanisms might operate at the same time, we did not want to assume that the driving mechanism was the same in all geometries.

In principle, we could then use the fit parameters to display the sum of only the imaginary parts of the fitted complex Lorentzian susceptibility for each mode in order to compare to traditional optical absorption spectroscopy. We have not done so here choosing instead to show the agreement of our fits to the experimentally derived Fourier power spectra.

5. Buried interface sensitivity: native-oxide-covered GaAs (100)

Even without detailed fitting, the spectrum in the right inset of Fig. 1 shows 3 clear spectral features. We examine these features more closely in Fig. 2. The left side of Fig. 2 shows the apodized power spectra for various injected carrier densities (i.e., pump fluence). The photoinjected carrier density at the sample surface is calculated using the literature values of the optical constants [54] integrated over the measured frequency spectrum of our femtosecond laser pulse. We fit the data to 3 modes (i.e., 12 unknowns). The highest frequency mode stays fixed at 8.80 ± 0.015 THz, the middle frequency mode shifts from 8.48 to 8.29 THz, and the lowest frequency mode shifts monotonically from 7.52 to 7.67 THz. The error bar is $\pm$ 0.004 THz in these fits due to nonlinear coupling with the other parameters. In order to see the two lower frequency modes more easily, on the right side of Fig. 2 we have plotted the apodized Fourier power spectrum of the oscillatory part of the SH signal, $S(t)$, minus the free-induction decay of the 8.80 THz mode deduced by fit. The $\sim$ 8.4 THz mode is clearly observed as well as the lack of remaining 8.80 THz mode susceptibility.

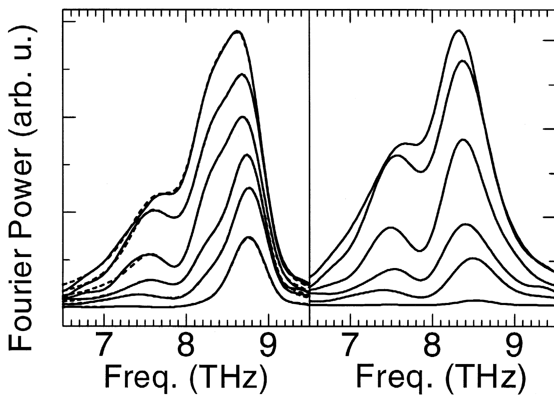

Fig. 2. (Left) Fourier power spectra of the TRSHG of native-oxide-covered GaAs (100). From smallest to largest amplitude curve, peak injected carrier densities were: 1.2, 4.8, 7.2, 11, 15, and 22 ($\times 10^{17}/\mathrm{cm}^3$). (Right) Fourier power spectrum of *S(t)* data minus the free-induction decay of the 8.80 THz mode obtained by fit.

The 8.80 THz mode is the well-known bulk LO phonon mode at $q = 0$. The mode itself is well studied by Raman spectroscopy and other techniques. Kurz and co-workers have studied this mode extensively by femtosecond time-resolved linear reflection and electro-optic measurements and shown that it is driven by the field-screening mechanism. At low injected carrier density the LO phonon motion has a frequency of 8.80 THz because carriers are swept out of the depletion region. At higher injected carrier density, the plasma mode of the carriers remaining in the depletion region or just beyond the depletion region couple to the LO phonon motion. The observed 7.5–7.67 THz mode is consistent with the frequency, frequency shift and dephasing time of the LO-phonon-electron-plasmon coupled mode [55]. As more electrons are injected the frequency shifts toward the bulk TO phonon frequency, 8.0 THz. Since these are bulk modes, we also observe them using femtosecond time-resolved linear reflectivity and similar results have been published by Kurz and co-workers [56].

The mode at ~ 8.4 THz is a local interfacial mode confined to a few monolayers of the interface. The data in Fig. 2 allow us to argue that it cannot be anything else. It cannot be a pure bulk mode. Our excitation region is the 140 Å deep depletion region over the ~ 20 μm laser spot diameter. Expansion of this motion as a superposition of pure bulk modes can only involve modes with $q_{\parallel} < 1$ $\mu\mathrm{m}^{-1}$ and $q_z < (1/200)$ Å^{-1} for which there is a gap between the bulk TO and LO phonon frequencies at 8.0 and 8.8 THz. The ~ 8.4 THz mode cannot be the bulk LO-phonon-electron-plasmon coupled mode which is observed at frequencies < 8.0 THz.

The ~ 8.4 THz mode cannot be a Fuchs–Kliewer mode. The F–K mode is a phonon mode coupled to the field induced by the interfacial charge oscillation that the phonon itself creates at the dielectric discontinuity of the interface. The Fuchs–Kliewer (F–K)

modes have a bulk LO phonon-like lattice displacement that is elliptically polarized and varies sinusoidally along the surface and exponentially into the bulk as $\exp(iq_{\parallel}x - q_{\parallel}z)$ [57]. The F–K mode is confined to the surface in the same way that a surface plasmon is coupled to the field induced by the surface current. For semiconductors, the F–K mode can also be strongly coupled to interface plasmon modes when the displacement vectors and frequencies are well overlapped. The Fuchs–Kliewer mode dominates HREELS measurements near the bulk LO phonon features. This is because the wave-function of the incoming electron in the impact regime is well-matched to the Fuchs–Kliewer mode displacement ($q_z \sim q_{\parallel}$). In our experiments, however, we can only excite modes with $q_{\parallel} < 1\ \mu m^{-1}$. The F–K excited modes would extend $> 1\ \mu m$ exponentially into the bulk. Since the SH only detects changes in the SH susceptibility in the top 150 Å, the SH suppresses detection of the F–K mode by > 70 compared to HREELS. The depletion-field-screening mechanism for driving the bulk LO phonons only applies over the 140 Å depletion region which is also poorly matched to the F–K mode. If the ~ 8.4 THz mode were spatially extended over $\sim 1\ \mu m$ depth, we would also expect to see it in time-resolved linear reflection measurements. We have not observed this mode nor have Kurz and co-workers.

In an earlier publication [6], we argued that the ~ 8.4 THz mode could not be the LO-phonon-hole-plasmon coupled mode. The topmost 25 Å of the interface is indeed hole-rich due to the separation of the photoinjected carriers in the depletion region. Raman studies in p-doped GaAs show the bulk LO-phonon-hole-plasmon coupled mode frequency shifts continuously from the LO frequency to the TO frequency as a function of hole density [58]. The frequency shift occurs abruptly between 4 and $7.5 \times 10^{18}/cm^3$ hole density. In subsequent TRSHG experiments on the GaAs (110)-native-oxide-covered surface we have found that there can be a strong LO-phonon-hole-plasma coupled mode oscillation at very high injected carrier densities and that frequencies as low as the TO phonon frequency 8.0 THz can be observed. However, in this experiment on the (100) surface at the lowest injected carriers ($< 0.5 \times 10^{18}/cm^3$) the observed feature cannot be due to the bulk LO-phonon-hole-plasma coupled mode. Using the most conservative argument, the peak hole amplitude at the interface is $< 5 \times 10^{18}/cm^3$ and the hole-plasma coupled mode at these densities should be > 8.5 THz. Since the bulk LO phonon amplitude is negligible at the interface the SHG from the coupled mode is derived from deeper layers for which the hole density is even lower. At the lowest injected carrier density, the interface mode at 8.48 THz dominates. At higher injected carrier density both the interface and bulk LO-phonon-hole-plasma coupled mode contribute. Detailed simulations of these bulk features will be published elsewhere.

Confining our attention to the features observed for in the two lowest injected carrier densities (1.2 and $4.8 \times 10^{18}/cm^3$), the measured mode frequencies are 8.48 and 8.45 THz, respectively. The dephasing times are 704 ± 140 and 618 ± 40 fs where the larger error bar of the former is due to the relatively small amplitude of the peak with respect to the noise. This dephasing time is relatively long when one considers possible disorder at the native-oxide interface that is well-known to be atomically abrupt but not epitaxial. We have argued on the basis of elimination that the mode must be due to an interface mode localized to the topmost 1–4 atomic layers (2 Ga and 2 As layers). This assignment is supported by the large body of results that follow on the monolayer sensitivity of the SHG signal, the clean surface spectra, and spectral changes during in situ oxidation.

6. Sensitivity to monolayer scale local phonons

To fully demonstrate the monolayer sensitivity of the TRSHG phonon technique, we investigated a number of clean GaAs surfaces in UHV. In Fig. 3, we show the Fourier power spectra of the apodized $S(t)$ for the GaAs (001) in the UHV chamber: (a) the intact native oxide, (b) after Ar^+ – ion sputtering and thermal annealing to 550°C to obtain a well-ordered (4 × 6) LEED pattern, and (c) after Ar^+ – ion sputtering at 500 eV at 77° angle of incidence corresponding to removal of ~ 1.1 GaAs monolayers assuming the yield was one atom per Ar^+ – ion. The crystal was oriented with the [011] axis in the plane of incidence. The pump was s-polarized. As shown in Tables 3 and 4, we should be able to excite only

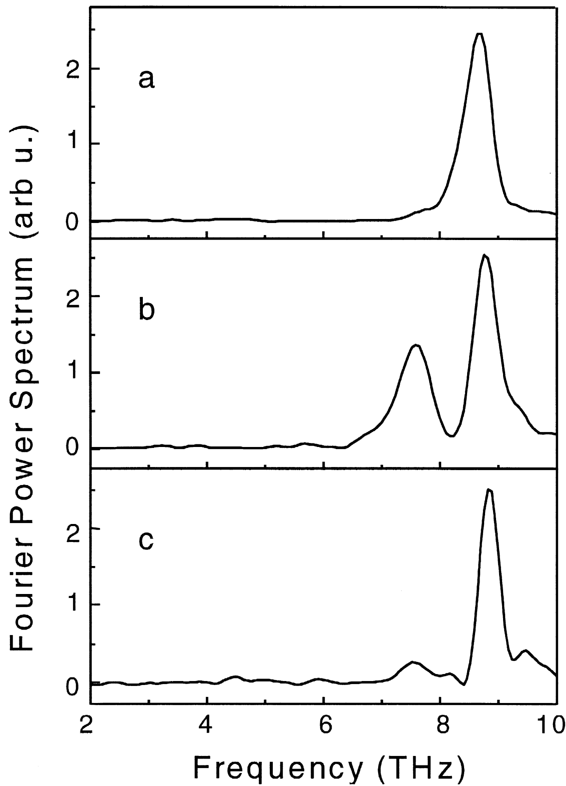

Fig. 3. Fourier power spectra of differential $p_{in} - p_{out}$ TRSHG for GaAs (100) oriented with [011] ∥ incident plane and *s*-polarized pump. (a) Native-oxide-covered interface, (b) after sputtering and thermal annealing to obtain (4 × 6) LEED pattern, (c) after Ar^+-ion sputtering to remove ∼ 1.1 monolayer equivalents.

A_1 modes in this geometry and therefore even though we could have detected both A_1 and B_1 modes by TRSHG, we should only see A_1 modes in the coherent phonon spectrum. In this and all subsequent results reported in this article, the injected carrier density is adjusted to be around 5×10^{17} cm^{-3}. This eliminated the possibility of detecting spectral features associated with the bulk LO-phonon-electron-plasma coupled modes between 7.5 and 7.8 THz and the bulk LO-phonon-hole-plasma coupled modes between 8.8 and 8.0 THz. The new spectral features are assigned to local surface phonon modes. The appearance of new interface-specific (surface) phonon features in curve B and their removal in curve C demonstrates that the technique is sensitive to the coherent phonon motion of a few monolayers of the surface – in this case the reconstructed surface layers. Examination of curves A and B in the vicinity of 8.45 THz is consistent with the assignment of the phonon at the native-oxide interface being localized to a few (1–4) monolayers of the surface. The 8.45 THz mode is removed when the oxide is removed. Only the pure bulk mode survives after sputtering in curve C. The Fuchs–Kliewer surface phonon for clean GaAs (100) has been observed in HREELS at 8.71 THz. Here a mode at 8.71 THz would be too close to the bulk LO phonon (8.76 THz) to be resolved because the spectral linewidth is ∼ 0.5 THz. As we have discussed above, however, we do not expect to see the Fuchs–Kliewer mode in TR-SHG.

In curve C, the bulk LO phonon peak persists but the phonon line width is about 30% larger and the peak height is 2 times lower (initial amplitude is 65% of the well-ordered clean surface). This change is presumably due to sputter-induced defect formation in the near surface bulk. In numerical simulations following Ref. [32], we find that the peak LO phonon displacement occurs in a broad maximum between 50 and 100 Å below the interface. The SH sensitivity is of course peaked at the surface. The change in spectral feature is consistent with removal of 3–4 atomic layers (3–4 atoms/Ar^+ ion) and defect formation with a penetration depth of 20–25 Å with 500 eV Ar^+ ions. The penetration depth of ∼ 600 eV Ar^+ ions has been previously estimated by AES to be ∼ 10–15 Å [59]. The sputter efficiency depends on the surface structure, local dipole moments and angle of incidence. The sputter rate may be more efficient in our case due to the atomic lattice strain induced by the reconstruction. The author of Ref. [59] was careful to measure the sputtering rate in steady state (no reconstruction).

7. GaAs (110)–(1 × 1)

In the bulk of zincblende-type compound semiconductors [110], layers consist of planar zigzag chains of alternating cations and anions along the [1$\bar{1}$0] direction [60]. When bulk-like terminated, each surface atom has 3 nearest neighbors instead of 4 and therefore has one broken or dangling bond. The

LEED pattern for the thermally annealed GaAs (110) surface shows a relaxed (1×1) structure. This is the simplest semiconductor surface reconstruction and therefore enormous experimental and theoretical attention has been applied to this reconstruction. Medium-energy ion scattering (MEIS) [61] revealed that the topmost zigzag chains were tilted with the As anions pointing outward and the Ga–As bond length was conserved. Scanning tunneling microscopy images verified the lateral arrangement [62]. To accommodate 3-fold sp^2-hybridized cations one expects a tilt angle of approximately 28° with respect to the surface plane. This is supported by a number of theoretical works which calculate the atomic structure and phonon spectrum using various approaches to obtain the interatomic force constants [63–69]. One expects that in addition to the top layer being tilted, lower layers will also be slightly tilted as the lattice distortion will propagate from the surface into the bulk. The reconstruction involves at least 3 atomic layers.

Recently the atomic and electronic structures and phonon spectra for several clean and adsorbate-covered semiconductor surfaces have been calculated using first principles (ab initio). For the GaAs (110)–(1×1), J. Fritsch, et al. [69] first determined the atomic relaxation geometry by minimizing the total energy in a slab configuration consisting of periodically repeated nine-layer slabs separated by vacuum equal to three layers. The surface electronic structure accompanying this calculation was published separately [70]. They determined the harmonic force constants of the fully relaxed nine-layer slab using a density-functional perturbation scheme and used those constants to model the dynamical matrices of a 25 layer slab. For modes dispersed along or perpendicular to the chains from the surface Γ-point, the calculation finds 3 acoustic modes and 6 nearly dispersionless optical phonon bands. All have A' symmetry.

Numbering the predicted optical modes from 1 through 6, the lowest frequency optical mode S1 is predicted to have frequency 3.98 THz and to be dominated by motion of the topmost Ga atom perpendicular to the chain (i.e., in the [100] and normal directions). The S2 mode at 5.80 THz is predicted to be dominated by the motion of the topmost As atom perpendicular to the chain. The S3–S5 modes at 7.37, 7.56, and 7.86 THz are predicted to be dominated by opposing Ga–As motion in Ga–As layers 2 and 3 parallel to the plane. The S6 mode at 8.36 THz is predicted to be dominated by the opposing motion of the topmost Ga and second layer As perpendicular to the chains.

Harten and Toennies used HAS to explore the low frequency modes [71]. They observed two surface acoustic modes with energies of 5.6 and 7.3 meV at the surface Brillouin zone. They also observed two flat bands with energies at 10 and 13 meV. In HREELS investigations [72,73] the Fuchs–Kliewer modes at 35.8 meV is observed to dominate the higher energies. In Ref. [68], 2 acoustic modes, 3 nearly dispersionless local optical modes 10.5, 16.5, and 21.5 meV, and the Fuchs–Kliewer mode were observed. The motion of the 16.5 and 21.5 meV (3.99 and 5.20 THz) were assigned to the S1 and S2 eigenfunctions found in Fritsch et al.'s ab initio slab model calculations.

Fig. 4 shows the TRSHG data taken in 4 excitation geometries for the GaAs (110) relaxed (1×1) reconstructed surface. The crystal was oriented either with the [001] or $[1\bar{1}0]$ in the plane of incidence and the pump either *s*- or *p*-polarized. The time-domain oscillations are shown on the left. The Fourier power spectra are shown on the right. The fits to the data are shown in dashed line in the figure and are essentially indistinguishable from the data (shown in solid line). In Table 5 we list fit values of mode frequencies and dephasing times as well as the mode frequencies from HREELS data [73], the ab initio calculation by Fritsch, et al. [69] and a tight-binding total-energy-minimization model calculation [66]. Other than the bulk mode at 8.76 THz, all the other modes are localized surface phonon modes. We observe 6 modes in excellent agreement with the number of modes and energies predicted in the ab initio calculation and we label our experimentally measured modes in the same manner as S1–S6.

We point out that even though there are apparent peaks in the Fourier power spectrum data at frequencies away from the mode center frequencies (shown with arrows), the fits still follow such features very accurately. For example, a feature with maximum power spectra amplitude at ~ 6 THz appears in curves B, C, and D. These features cannot be caused by subtraction errors or noise because it is unlikely

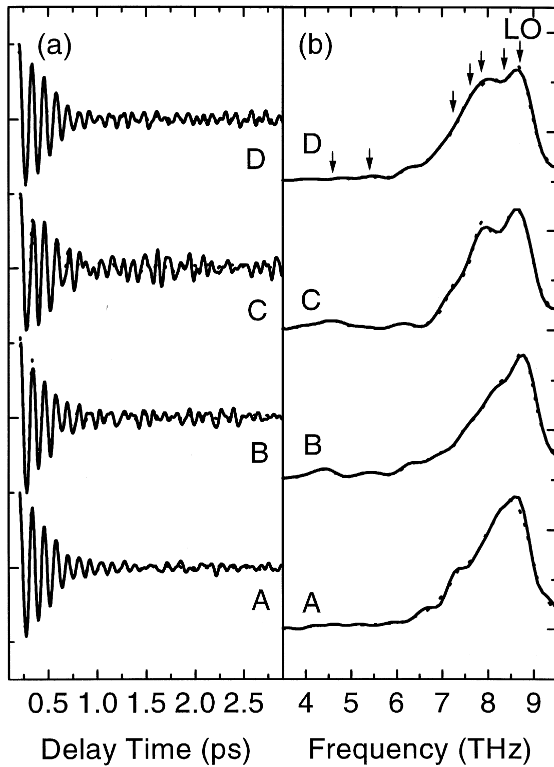

Fig. 4. Differential $p_{in} - p_{out}$ TRSHG for GaAs (110) (1×1) surface. (a) *S(t)* vs. pump–probe time-delay and (b) Fourier power spectra of *S(t)* for 4 geometries. A: [001] ‖ plane of incidence, *s*-pol. pump. B: [001] ‖ plane of incidence, *p*-pol. pump. C: [1$\bar{1}$0] ‖ plane of incidence, *s*-pol. pump. D: [1$\bar{1}$0] ‖ plane of incidence, *p*-pol. pump. Data in solid lines and results of curve fitting in dashed lines. Arrows show phonon frequencies obtained from fit.

that they could be reproduced so accurately with a simple analytical function. These off-line-center features occur because of the interference between the complex Lorentzian modes and we have chosen to display the Fourier power spectra rather than to display individual phases of the complex Fourier transform. We could have optomized the display for one mode by displaying the phase of the complex Fourier transform that shows only the imaginary part of the Lorentzian susceptibility. This choice would allow that one mode to be easily distinguished in all 4 curves. However, this choice could only be optomized for one mode at a time. We have confidence in the fitted values of the mode frequencies and dephasing times because these parameters are constrained to fit all 4 spectra (different linear combinations of modes) simultaneously.

Our S1 mode at 4.57 THz is just above the range of the feature at 3.99 ± 0.4 THz peak measured in HREELS and above the ab initio calculation. The tight-binding calculation also predicts a 4 THz mode but instead the phonon displacement is dominated by bond-length preserving rotation-like motion of the topmost Ga and As atoms in the direction perpendicular to the chain. We may be detecting the same mode as in the HREELS measurement or may be detecting an additional mode that is dominated by in-plane motion and therefore suppressed in HREELS.

The S2 mode at 5.41 THz matches the value measured in HREELS and agrees relatively well with the ab initio calculation. Our measured value also agrees with the tight-binding model calculation which finds two shear modes of the topmost Ga and As atoms parallel (*1A″* at 5.32 THz) and perpendicular ($q_{\|}$ at 5.56 THz) to the zigzag chain direction [1$\bar{1}$0].

As shown in Tables 3 and 4, only A' modes can be detected by SH when the $x = [001]$ axis is in the

Table 5
Coherent phonon modes detected on GaAs (110)–relaxed (1x1) surface

N	υ_n (THz)	T_n (fs)	Sym.	υ_n (THz) Exp't [73]	υ_n (THz) Theo [69]	υ_n (THz) Theo [66]
S1	4.57 ± 0.05	790 ± 140	A'	3.99 ± 0.4	3.98	3.94
S2	5.41 ± 0.04	600 ± 150	A'/A''	5.20 ± 0.25	5.80	5.32
						5.56
S3	7.29 ± 0.03	550 ± 30	A'	–	7.37	–
S4	7.58 ± 0.01	720 ± 50	A'	–	7.56	–
S5	7.85 ± 0.01	470 ± 10	A'	–	7.86	–
S6	8.35 ± 0.07	800 ± 30	A'	–	8.36	–
B	8.76 ± 0.01	740 ± 80	–	8.76	bulk LO	

plane of incidence. Appearance of a mode in curves A or B allow us to identify it as A'. Both A' and A'' modes can be detected when the $y=[1\bar{1}0]$ axis is in the plane of incidence. The appearance of a mode only in this geometry (curves C and D) is necessary but not sufficient to identify the mode as A''. We required that in order to be 'not observed' in A or B, the fit value of the amplitude had to be less than the noise level in both curves and found that only our S2 mode could be A'' as noted in Table 5.

We observe the 3 modes, S3–S5, with extraordinary agreement with the mode frequencies predicted by the ab initio calculation. The calculation predicts this motion to be dominated by in-plane motion in the second and third layers. These modes are observed to have A' symmetry in agreement with the ab initio calculation. A' modes (as shown in Tables 1 and 2) have IR transition moments in both the z and x directions. Because the motion is largely in plane, the induced dipole moment in the z direction is probably relatively small compared to that in the x direction. These modes were probably not observed in HREELS because in the impact regime, HREELS is insensitive to dipole moments parallel to the surface.

One might expect that optical probes would also have the same insensitivity to parallel motion. This is true for linear (IR) probes especially on metals where the parallel field at the surface is greatly reduced. However, for nonlinear optics, the response is due to a tensor susceptibility with a richness that offers elements that can be sensitive to parallel motion. For example, elements with component projections such as $\partial\chi^{(2)}_{zzx}/\partial Q_x$ can generate SH polarization $P_z(2\omega)$ perpendicular to the surface due to phonon motion Q_x parallel to the surface. The strong S3–S5 peaks demonstrate that TRSHG can indeed detect motion parallel to the surface. Detection of motion perpendicular to the surface is of course always allowed due to symmetry breaking in the z direction.

The S6 mode at 8.35 THz also agrees well with the ab initio calculation. This mode should have a strong dipole moment projection normal to the surface but is not observed in HREELS because of the dominance of the Fuchs–Kliewer mode.

We note that the resolution and uncertainty in the assignment of the center frequencies of the modes are comparable or better than for HREELS. This is possible despite the large number of overlapping features because we simultaneously fit 4 linear combinations of the modes. We use a single set of ν_n and T_n to fit the 4 data sets simultaneously so the number of free parameters is drastically reduced. In principle, this can be further improved by measuring the phonon spectra in even more excitation geometries. For purposes of fitting the spectra, this approach is far better than averaging a longer time to get better S/N on a smaller number of spectra. One could have probably improved the fits even more by using the same data collection time but generating 8 linear combinations and only sacrificing $\sqrt{2}$ in the S/N. However, this approach only works if the mode is detected in those 8 geometries, i.e., for fully symmetric modes. High S/N in individual curves is needed to determine the symmetry of non-fully-symmetric modes.

8. GaAs (100)–(1 × 6) and –(4 × 1)

The GaAs (100) surface is used in the photonic and semiconductor industries and has been studied by numerous surface techniques for almost three decades. Unlike the (110) surface, the (100) surface consists of alternating layers of Ga and As atoms so Ga and As dimerization is expected. The surface reconstructions depend critically on the preparation procedure. The surface structures are identified by their low energy electron diffraction (LEED) patterns [53,74,75]. According to an early work [53], the reconstruction progresses from $c(4\times4)$ As-rich (400°C), (2×4) or $c(2\times8)$ As-rich (450°C), (1×6) As-rich (500°C), (4×6) Ga-rich (520°C), (4×1) Ga-rich (540°C), to $c(8\times2)$ Ga-rich (550-600°C) and is reversible. On the basis of AES calibrated against the assignment of 0.5 ML on the GaAs (110)–(1×1), the As concentration was reported to be 0.61, 0.52, 0.27, and 0.22 ML for the c(2×8), (1×6), (4×6), and c(8×2) Ga reconstructions, respectively [53]. As pointed out in later works, the AES spectrum is sensitive to the exact locations of the atoms within the layers and the bulk stoichiometry cannot be assumed for underlying layers [76], but it is well accepted that annealing at higher temperatures reduces the surface As concentration.

STM studies by Biegelsen, et al. have greatly clarified the unit cell lateral structures that produce the LEED patterns [77], while leaving still controversial some details of the atomic arrangement. The surface identified as (1×6) in LEED has a (2×6) unit cell containing 2 As dimer and 4 As dimer vacancies aligned along the $[0\bar{1}1]$ and arranged along the [011] $(\times 6)$ direction (see Fig. 3 of Ref. [77]). In the $[0\bar{1}1]$ $(2\times$ direction), the dimers are stacked in a staggered 'chain' of dimers with alternating [010] and [001] displacement. In the missing As dimer 'trough' the second layer Ga are believed to form 2 dimers per (2×6) unit that are similarly staggered but oriented along [011]. The reported 0.52 ML As coverage is consistent with the equal numbers of As and Ga dimers per (2×6) unit cell. We annealed at 500°C and observed a sharp $(1 \times 6) + (1/6)nY^*$ LEED pattern. STM reveals that these streaks are from stacking disorder along the $[0\bar{1}1](2\times)$ direction. A (4×12) arrangement of (4×2) units is proposed for the $(1 \times 6) + (1/4)nY^*$ structure [78] but we were careful to note that only the $(1/6)nY^*$ streaks were observed in our study.

We prepared our (4×1) reconstructed surface by short anneals at 540°C which is just slightly higher than necessary to make the (4×6). We annealed just enough until we observed no (1×6) lead spots, no $(1/6)nY^*$ streaks, and no $(1/2)nY^*$ streaks or $c(8 \times 2)$ spots. A clean (4×1) LEED pattern can be produced at lower temperature than the $c(8 \times 2)$ [79] but in much of the literature the (4×1) LEED pattern is said to be accompanied by weak $c(8 \times 2)$ features and therefore the structure is considered a disordered $c(8 \times 2)$ [80]. In Biegelsen's STM study the (4×1) is considered a disordered $c(8 \times 2)$. The $c(8 \times 2)$ consists of (4×2) unit cells of Ga dimers and vacancies which are arranged along the $(4\times)$ or $(8\times)$ direction with a one unit cell stagger in the $(\times 2)$ direction. When the two (4×2) cells are not staggered then they have (4×2) periodicity resulting in the (4×1) LEED structure. Biegelsen, et al. proposed that the (4×2) cell contained 2 dimers and 2 vacancies both oriented along the [110] $(\times 2)$ direction and arranged along the $[0\bar{1}1](4\times)$ directions [77]. This structure is calculated to be the most stable configuration [81] and follows both Chadi's missing dimer model [82] and Pashley's electron counting model [83]. Recently a LEED I–V curve analysis of the $c(8 \times 2)$ suggested that the basic (4×2) cell consisted of 3 inequivalent Ga dimers and 1 Ga dimer vacancy [84]. In the proposed structure the central dimer is fully dimerized and significantly compressed toward the surface while the two outer dimers are about half-dimerized and the backbonds are only slightly modified compared to the bulk. If the latter case is true, then there may be a 'true' LEED (4×1) structure with a (4×2) cell containing 2 Ga dimers and 2 vacancies as the As concentration decreases in a continuous manner from the (1×6) through the combination (4×6) to the (4×1) structure. The STM image contrast of the dimers in the '4×1' and $c(8 \times 2)$ arrangements appears the same so there is no evidence in STM of a different local configuration for the two LEED patterns. However, in examining the STM figures, it seems surprising that there are no differences caused by strain in the underlying layers. We wanted to compare the clean (4×1) surface to the $c(8 \times 2)$ in order to comment on this controversy but found that our experimental setup could not reach high enough temperatures to produce a high quality $c(8 \times 2)$ reproducibly. In either case the (4×1) structure is dominated by the local (4×2) structure with only Ga dimers on the top layer.

In Fig. 5 we show the Fourier power spectra of the TRSHG data for the clean GaAs (100) surface with (1×6) As-rich and (4×1) Ga-rich reconstructions. We measured 4 excitation geometries with the sample oriented either with the crystalline [011] or $[0\bar{1}1]$ parallel to the plane of incidence and the pump-pulse either *s*- or *p*-polarized. Clear differences between the (1×6) and (4×1) surfaces are observed in the spectra, but the same number of modes seems to appear. There are 4 modes between 6 and 8.5 THz. All 4 modes appear in curves A and C. Examination of Tables 3 and 4 allows us to conclude that the 4 detected modes must have A_1 symmetry. The fitting results are shown in Table 6.

There also appear to be at least 2 modes at approximately 4 and 5 THz on both surfaces, but we have not listed values for them in Table 6. At the largest those mode amplitudes are only a factor of 2–3 over the noise so the fits for those features cannot be meaningfully constrained by requiring simultaneous fitting of the 4 curves. Because they appear in curve A for the (1×6) and curve C for the

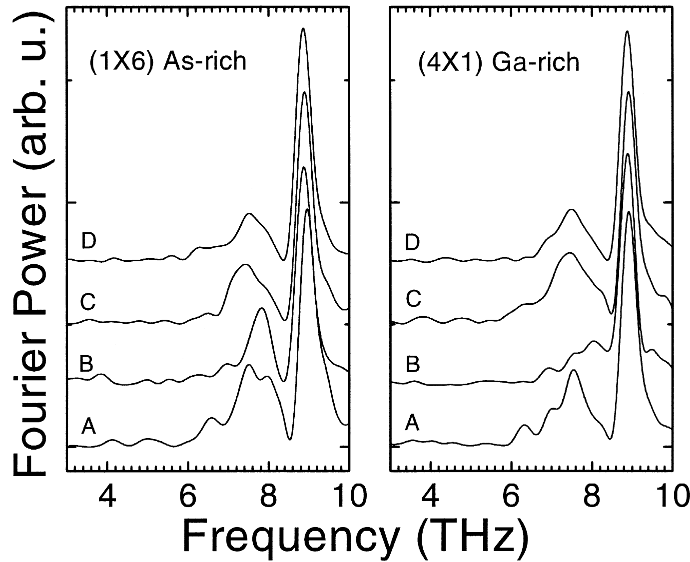

Fig. 5. Fourier power spectra of p_{in}–p_{out} TRSHG from GaAs (100)–(1 × 6) As-rich and (4 × 1) Ga-rich reconstructions. A: [011] ∥ plane of incidence, *s*-pol. pump. B: [011] ∥ plane of incidence, *p*-pol. pump. C: [0$\bar{1}$1] ∥ plane of incidence, *s*-pol. pump. D: [0$\bar{1}$1] ∥ plane of incidence, *p*-pol. pump.

(4 × 1), these modes must have A_1 symmetry and therefore result in dipole moments perpendicular to the surface (T_z).

HREELS of the GaAs (100)-c(8 × 2) shows three features at 7.9, 11.5, and 35.8 meV (1.9, 2.78, and 8.66 THz, respectively) [85]. The latter is the Fuchs–Kliewer phonon mode. The modes we observe are therefore not observed in HREELS, presumably for similar reasons as on the (110) surface. Since these are all A_1 modes, the T_z must be too small to detect by HREELS above the wings of the F–K mode.

Unfortunately, there are no calculated phonon spectra with which to compare. The (100) reconstructions involve far more atoms than the (110)–(1 × 1) so such calculations are non-trivial. However it is tempting to speculate about the mode displacements on the (100) surface by comparing to the eigenfunctions calculated for the (110). The 4 modes from 6–8.5 THz all have frequencies near the bulk LO phonon frequency and are probably due to Ga–As counter-propagating motion as opposed to adatom or dimer motion. The highest lying phonon mode at ∼ 8.15 THz is probably dominated by out-of-plane counter-propagating motion of the Ga-As bond between the dimer and second layer or second and third layers below the dimers. Because the induced polarization of the lattice motion is also in the

Table 6
Coherent phonon modes detected on GaAs (100)–(1X6) As-rich and –(4X1) Ga-rich reconstructed surfaces

N	(1X6) As-rich			(4X1) Ga-rich		
	υ_n (THz)	T_n (fs)	Sym	υ_n (THz)	T_n (fs)	Sym
S1	6.46 ± 0.55	1040 ± 250	A_1	6.20 ± 0.66	960 ± 160	A_1
S2	7.46 ± 0.01	1000 ± 180	A_1	7.19 ± 0.05	690 ± 50	A_1
S3	7.80 ± 0.01	570 ± 10	A_1	7.63 ± 0.02	1040 ± 60	A_1
S4	8.15 ± 0.04	480 ± 20	A_1	8.12 ± 0.02	480 ± 10	A_1
B	8.81 ± 0.01	2630 ± 90	–	8.80 ± 0.01	2730 ± 150	–

direction of the displacement (along z), the vibrational frequency will be shifted above the intrinsic frequency in the same way that the LO phonon frequency is higher than the TO phonon frequency. The intrinsic mode frequency might be expected to be lower than the value of 8.36 THz found on the fully relaxed (110) surface because the Ga–As backbonds are stretched and therefore weakened in order to accommodate the As–As or Ga–Ga dimerization.

The 3 other modes from 6–8 THz are probably dominated by in-plane motion of the underlying 2–4 layers. The basic structure of these layers is the same in the two reconstructions, however, the strains are different. Examining the dephasing times in Table 6 we note that 2 modes have extremely long dephasing times of order 1 ps. This is rather surprising considering the possible inhomogeneity of the (4×1) reconstructed surface. By comparison, the dephasing times of the bulk LO phonon, the buried native-oxide-covered interface phonon at this low injected carrier level, and the longest lived phonon on the (110)–(1×1) are 2.6, 0.7, and 0.8 ps, respectively. A phonon mode dominated by the motion of the topmost 2 layers would be strongly damped by coupling to the surface state. It is therefore likely that the long-lived 6.20 and 7.63 THz modes on the (1×6) and 6.46 and 7.46 THz modes on the (4×1) are localized on the third and fourth layers with most of the displacement amplitude arranged symmetrically in-plane. These two modes would be rather similar except for the strains induced by the upper 2 layers. Like two coupled oscillators, the two long-lived modes may be split in energy by having displacements dominated by relatively more or less amplitude under the dimer or dimer vacancies.

The remaining modes at 7.19 THz on the (1×6) and the 7.80 THz on the (4×1) have short lifetimes and are probably strongly coupled to the surface electronic structure or the disorder in the first 2 layers of the reconstructions. In analogy with the (110)–(1×1) modes we can speculate that these modes are dominated by counter-propagating in-plane motion of the backbonds directly below the dimers (between layers 1 and 2).

Finally, in analogy with the two low frequency modes on (110)–(1×1), the 2 or more low frequency modes in the 3–6 THz range on clean (100) are probably shear, stretch, wag, or rotation of the topmost dimers. Unfortunately, we did not have enough S/N to detect those modes reliably. If they are dimer modes, then they are probably well-coupled to the surface electronic structure, especially the dangling bond states, and therefore short-lived, spectrally broad, and hard to detect.

9. Adsorbate and chemical reaction sensitivity: in situ oxidation

In Fig. 6 we demonstrate the chemical sensitivity of the TRSHG phonon technique. We oxidized the GaAs (100)–(4×6) reconstruction in UHV. LEED and STM [77] are consistent with this surface having domains of both the (1×6) and (4×1) Ga-rich reconstructions. We prepared the (4×6) by annealing at 520°C so this structure should not be confused with the highest Ga concentration (4×6) reported by Xue, et al. [86]. Although our (4×6) is not a single domain surface, it is adequate for showing the chemical sensitivity. On the left of Fig. 6, we show the Fourier power spectrum of the apodized oscillatory TRSHG and on the right we show the same data except we have subtracted the best fit bulk LO phonon feature at ~ 8.8 THz (the same way we did

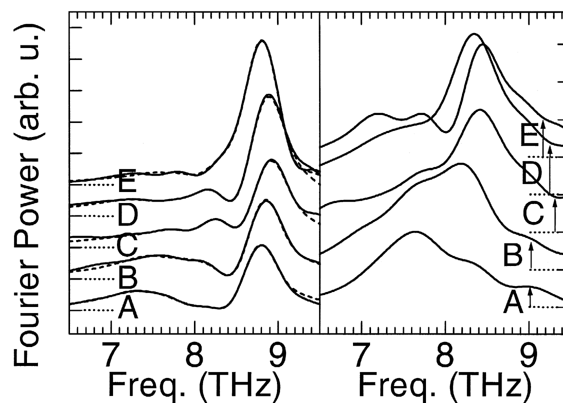

Fig. 6. Fourier power spectra of clean GaAs (100)–(4×6) vs. O_2 exposure (Langmuir). Left: Power spectrum of $S(t)$ data. Right: Power spectra of $S(t)$ data minus the fitted free-induction decay of the 8.80 THz mode. (A) clean surface, (B) 10^2 L, (C) 10^4 L, (D) 10^6 L, (E) native-oxide-covered surface in UHV chamber. The injected carrier density was $1.8 \times 10^{17}/cm^3$. Data (solid) and fit (dashed). Curves are offset vertically by tick mark units.

in Fig. 2). The spectra are normalized with respect to the best fit bulk LO phonon oscillation which we presume to be constant. Curve A is the clean (4×6). Curves B–D are obtained after progressively 10^2, 10^4 and 10^6 L O_2 exposure. Molecular oxygen is backfilled into the UHV chamber in the presence of a lit nude ion gauge filament. Because the (4×6) is a mixed domain surface, curves A–D are obtained in a single run. The native-oxide data (curve E) was measured in the UHV chamber with nominally identical laser conditions as for curves A–D but before the oxide was removed and the surface was cleaned. The progression from curve A–D clearly shows submonolayer sensitivity to chemical and structural changes associated with adsorbates.

Many groups have studied the adsorption of oxygen on GaAs surfaces. At room temperature and up to 100°C, temperature programmed desorption spectroscopy (TPD) [87] and helium diffraction studies [88–90] have shown that molecular O_2 adsorbs and creates defects at which subsequent adsorbed O_2 can dissociate and then bond atomically. The Ga–O bond is energetically preferred because the surface dimerization creates empty dangling bonds for surface cations [79,80] which can be filled by the π^* electrons on an oxygen atom and form Ga–O bonds [91–93]. An ab initio calculation of O atom chemisorption on reconstructed GaAs (100) finds that the minimum energy configuration occurs when the O atom is in a nearly bridge-bonded position between two Ga atoms [94]. The Ga atoms are distorted 0.40 Å from their bulk-terminated ideal locations which strains the underlying semiconductor layer significantly. The O atom is also displaced with respect to the ideal vertical bridge position in both in-plane dimensions. This symmetry breaking even at the first oxide layer causes subsequent oxide layers to be amorphous. While this calculation predicts the minimum energy configuration, it does not take into account the dynamics or coverage dependence related to O_2 molecule dissociation. Recent AES studies suggest that the initial oxidation state at low coverage ($< 10^4$ L without electronic excitation due to filaments) proceeds by oxidizing both Ga and As [95]. If that were the case, the simultaneous As oxidation could occur by oxidizing the As backbonded to the Ga dimer on the (4×1) at the same time the Ga dimer is oxidized. Alternatively, oxidation could occur simultaneously on the As dimers on (1×6) domains and Ga dimers on (4×1) domains.

Adsorption with a lit filament is known to proceed more efficiently than oxidation without a lit filament because the filament-excited-O_2 molecules can dissociate more easily on the surface. The authors of Ref. [80] reported that in the presence of a cold cathode ion gauge (lit filament) the sticking coefficient was enhanced by 4 orders of magnitude, i.e., from 10^{-9} to $\sim 10^{-5}$ and that under those conditions a saturated 0.5 ML was obtained in 10^6 L. They found that the (110)–(1×1) oxidized at the same rate as the (100)–(4×1) with the filament lit. We used a lit nude ion gauge. In SH intensity vs. O_2 exposure studies in the same experimental configuration on GaAs (110)–(1×1) we found that we oxidized the dangling bonds with Langmuir kinetics at the rate of $(1200\ \mathrm{L})^{-1}$ and then oxidized the backbonds at least 100 times slower after the initial phase. We therefore expected the (100)–(4×6) to oxidize at a similar rate and to saturate at 0.5 ML well before 10^6 L gas exposure.

The room temperature native oxide layer is about 50–80 Å thick. The oxide layer is stoichiometrically correct but is structurally amorphous. X-ray photoelectron spectroscopy shows that oxides grown at room temperature contain As-oxides, primarily As_2O_3 as evidenced by As^{5+} and As^{3+} XPS lines [96]. Raman scattering shows that elemental As is only found in native oxide layers grown at or heat-treated at elevated temperatures [97–99]. We obtained our native-oxide-covered surface spectra before applying heat.

Because of the excited oxygen, we expect both molecular and dissociated O atoms are adsorbed even at the lowest exposures at a rate comparable to $1200\ \mathrm{L}^{-1}$. We see that in curve B, after only 100 L of exposure, there are significant changes in the surface phonon spectrum. The 8.2 THz mode grows while the other modes remain constant. The 8.2 THz mode continues to grow and saturates in amplitude by 10^4 L. Also in the 6.5–8 THz range, the broad feature in curve A centered at 7.6–7.7 THz seems to be redistributed in a way that roughly preserves total oscillator strength. Both spectral changes are consistent with an efficient oxidation process that is saturated by 10^4 L. These changes are consistent with our earlier speculation that the 8.15 and 7.80 THz

modes of the (4×1) and 8.12 and 7.19 THz modes on the (1×6) were dominated by counter-propagating motion of the top-layer dimer and second-layer atoms. Oxidation should relax the backbonds and thus significantly change those lines. However, the other relatively narrow spectral features which we have tentatively assigned to in-plane motion in the third and fourth layers would be only shifted and broadened but maintain their oscillator strength. The spectra are not sufficiently resolved to distinguish whether the (1×6) or (4×1) oxidizes at a different rate but the data are consistent with oxidation of the dimers being saturated by 10^4 L.

Between curves C and D the 6.5–8 THz modes are hardly changed but the 8.4 THz mode is shifted and broadened. This might be due to oxidation of backbonds after the dimers are initially oxidized or might be due to oxidation of As dimers on the (1×6) which might have a different adsorption rate than the (4×1). The authors of Ref. [95] suggest that molecular oxygen can substitute for As dimers releasing elemental As that can be oxidized efficiently. Another possibility is therefore oxidation of the elemental As and the exposed second-layer Ga on the (1×6) reconstructed surface.

Between curves D and E, the most dramatic change is that the mode amplitudes in the 6.5–8 THz range are reduced to the level of the noise (see the zero-level indicated on right vertical tick-marks of plot). On the native-oxide-covered surface, oxygen has penetrated 50–80 Å into the bulk and the counter-propagating in-plane modes of the interface are probably so inhomogenously broadened as to be undetectable. However, the native-oxide interfacial mode at ~ 8.5 THz is still visible with the same amplitude as observed with the first 0.5 ML of adsorbed oxygen.

The local phonon mode of the native-oxide-covered interface must be localized within the topmost 1–4 layers (2 layers of Ga and As atoms) in order for the mode to remain essentially the same after only 0.5 ML of oxygen adsorption. It must either involve Ga–O bonds directly or Ga–As counter-propagating out-of-plane motion that is modified by the first 0.5 ML of oxygen adsorption. If molecular oxygen can bind substitutionally for the As dimer (as speculated by authors of Ref. [95]) then the oxidation of the (1×6) could expose Ga atoms and form the same energetically favored Ga–O–Ga bond structure that should form on Ga dimers on the (4×1). The ab initio calculation [94] of the bridge-bonded oxide predicts a relatively large electronic charge on the O-atom in the ground state. The surface state bandgap is larger than the bulk and both the highest-lying occupied surface state and lowest-lying unoccupied surface state overlap the corresponding bulk bands. Thus the counter-propagating Ga–O motion would have a large z-dipole moment. Moreover, the proposed position of the O-atom is laterally asymmetric with respect to the ideal bridge site and compressed normal to the surface. Under electronic excitation (typically to a more delocalized state), the atoms will be accelerated to a more symmetric and relaxed configuration and this electronic transition should have a reasonably large electron-phonon coupling. Since the native oxide of GaAs (100) is known to be disordered and non-epitaxial, it is very surprising to find a sharp interfacial phonon mode feature at the interface. It seems more likely that a molecular scale vibrational mode either directly at or below the Ga–O–Ga interface species would be sufficiently well-ordered on a local level to have a narrow spectral feature. The frequency can be above the bulk TO phonon frequency because of the polarization enhancement in the z-direction. It seems less likely that the 8.48 THz mode could be due to the parallel motion of the third or fourth layer of the reconstruction. Such motion would have to average the inhomogeneities of the first 2 layers and would lead to a broader feature than observed. Moreover, the strain would have to be extremely large on average to raise the 'bare' force constant to a level much greater than the bulk TO phonon frequency.

10. Discussion and conclusion

Examination of the A–B and C–D pairs of data in Figs. 4 and 5 show that when the pump laser is changed from s- to p-polarization the amplitude of the coherent surface phonons changes relative to the bulk phonon amplitude (which should not depend on polarization). Only SRE and MGR mechanisms can depend on the polarization of the laser beam-DECP and 'field screening' depend only on the number of

electrons excited. Thus all surface modes we detected on clean GaAs were driven at least in part by SRE or MGR mechanisms. Since all material systems have Raman active modes, the TRSHG technique should be applicable to all material systems provided the signals are large enough to detect.

For both SRE and MGR, the detected signal amplitude is proportional to the Raman susceptibility and to the hyper-Raman susceptibility. Because both tensors are unknown, it is premature to infer specific information about the relative amplitudes of various surface modes. However, it is very clear that the SH oscillation signals for the coherent surface phonons are extraordinarily large – the peak heights appear in the spectra 2–5 times smaller than the bulk LO phonon signal. Because the surface phonons have shorter dephasing times however, the initial amplitudes are comparable within a factor of 2 to the bulk LO phonon signal. We calculated the field screening dynamics in the depletion region following Ref. [32] and found the bulk LO phonon amplitude to be a maximum of 0.01 Å with a broad maximum from 50–100 Å depth and falling rapidly toward the surface and back of the depletion region. The surface phonons must be localized to ~5 Å, which is 10 times fewer atomic layers. Moreover, the Raman cross-section per layer for the bulk is 40 times too small to produce the same amplitude generated by field screening. The ratios of the two susceptibilities and the peak displacements must give a factor of 400 enhancement for the surface. We expect some enhancement compared to the bulk because the electron-phonon interaction is stronger due to 2-d confinement. We have also found that the SH is enhanced at the laser fundamental by resonance with the highest lying occupied dangling bond to lowest lying unoccupied dangling bond interband transition on the clean surfaces [70]. The SH intensity is about 10 times higher on clean surfaces than on the native oxide. Interface electronic transitions have been observed by optical second-harmonic generation spectroscopy at the GaN/GaAs (100) [100], ZnSe/GaAs, and Si–SiO_2 interface [101,102] and are near the bulk transitions. The ab initio calculation indicates that the semiconductor side of the oxide interface will be highly strained so a localized electronic state should be formed and it will have a gap slightly larger than the bulk [94]. The transition should therefore be resonantly enhanced at the pump and probe laser frequency and have a large electron-phonon coupling. A ~20× enhancement in both tensors on both the clean and oxidized surface is therefore reasonable. So despite the large signal, the surface atomic displacement is likely only ~0.005 Å.

In comparison to HREELS, TRSHG can detect modes with displacements parallel to the surface, has frequency resolution comparable and in many cases superior to HREELS (of order 1% energy bandwidth), and can detect modes near the Fuchs–Kliewer mode which typically dominates semiconductor HREELS in this frequency range. Although this technique can only obtain spectra at the center of the Brillouin zone, the ability to detect all the optical modes with sufficient resolution is an important advantage, especially on complicated reconstructed surfaces or at buried interfaces. TRSHG can be an important tool in the next decade in providing new data that will drive improvements in the theory and large-scale calculation of interface structure and dynamics. As suggested by these experiments, the optical phonon mode spectra are still a unique probe of the dynamics of the underlying atomic layers of reconstructions and are invaluable as a final check on the accuracy of electronic and atomic structure calculations.

The most intriguing spectroscopic possibility for TRSHG is to explore localized modes at buried interfaces. As pointed out before, only 1 case of a monolayer-scale localized phonon mode was reported for Sb monolayers on GaAs. Here we reported the second case: an interfacial mode buried under 50–80 Å of oxide. We observed that the driving mechanism had Raman symmetry and therefore the driving mechanism is generally applicable to clean and buried interfaces. We therefore expect TRSHG to be especially useful in the study of strained interfacial layers in semiconductor device and heterostructure geometries.

In the future, we hope to exploit the coherent control of phonons to study surface phonon coupling to other phonons, carriers, and surface adsorbates. Nelson and co-workers demonstrated control of the amplitude of a selected phonon mode in α-perylene molecular crystals [103]. Kurz and co-workers demonstrated the coherent control of bulk LO phonons in GaAs (100) [104]. The same should be

possible with surface and interface phonons and such multi-pulse pumping experiments are currently underway in our laboratory. We also hope to use the ultrafast time-resolution to see changes in the lifetime or frequency of the phonon modes due to coupling to transient electronic or phonon excitations [105,106].

On a purely spectroscopic front, we are also currently investigating the sensitivity of this technique on metal and insulator interfaces. To this end we have recently improved the signal to noise by a factor of $\sqrt{8}$ compared to the data shown here so we obtain $S/N = 0.94\times$ the shot noise limit for GaAs. This was accomplished by reducing the laser and non-optical electronic background noise by increasing the time-delay scanning rate from 1 to 30 Hz, using a more stable diode-pumped frequency-doubled Nd:YAG laser instead of an Argon ion laser as the pump for the fs Ti:Sapphire oscillator, and using pulse discriminator electronics to condition the photomultiplier output. For 512 delay times, we can obtain a S/N of 10 for the surface phonons on GaAs (enough to see essential features) in 2.4 m and S/N of 50 (as shown in the data in this paper) in 1 hour. Further improvement can be obtained by increasing the optical throughput and using more efficient photo-detectors.

Acknowledgements

The authors gratefully acknowledge support under National Science Foundation grant #CHE-9707143.

References

[1] F. de Witte (Ed.), Surface Phonons, Springer Series in Surface Sciences, Vol. 14, Springer, Heidelberg, 1988.
[2] T.A. Germer, J.C. Stephenson, E.J. Heilweil, R.R. Cavanagh, Phys. Rev. Lett. 71 (1993) 3327.
[3] P. Zhdanov, Surf. Sci. 197 (1988) 35.
[4] J.C. Tully, M. Gomez, J. Vac. Sci. Technol. A 11 (1993) 1914.
[5] Y.M. Chang, L. Xu, H.W.K. Tom, Phys. Rev. Lett. 78 (1997) 4649.
[6] Y.M. Chang, L. Xu, H.W.K. Tom, Phys. Rev. B 59 (1999) 12220.
[7] H. Ibach, D.L. Mills, Electron Energy Loss Spectroscopy and Surface Vibration, Academic Press, New York, 1982.
[8] J. Kroger, S. Lehwald, H. Ibach, Phys. Rev. B 55 (1997) 10895.
[9] J.P. Toennies, in: F. de Witte (Ed.), Surface Phonons, Springer Series in Surface Sciences, Vol. 14, Springer, Heidelberg, 1988, p. 248.
[10] G. Lange, J.P. Toennies, P. Ruggerone, G. Benedek, Europhys. Lett. 41 (1998) 647.
[11] R. Matz, H. Lüth, Phys. Rev. Lett. 46 (1981) 500.
[12] L.H. Dubois, G.P. Schwartz, Phys. Rev. B 26 (1982) 794.
[13] Ph. Lambin, J.P. Vigneron, A.A. Lucas, P.A. Thiry, M. Liehr, J.J. Pireaux, R. Caudano, T.J. Kuech, Phys. Rev. Lett. 56 (1986) 1842.
[14] V. Polyakov, A. Elbe, J.A. Schaefer, Appl. Phys. A 60 (1995) 567.
[15] T. Tsuruoka, Y. Uehara, S. Ushioda, T. Kojima et al., Surf. Sci. 368 (1996) 185.
[16] M. Liehr, P.A. Thiry, J.J. Pireaux, R. Caudano, Phys. Rev. B 34 (1986) 7471.
[17] P. Senet, Ph. Lambin, A.A. Lucas, Phys. Rev. Lett. 74 (1995) 570.
[18] C. Thompsen, H.T. Grahn, H.J. Maris, J. Tauc, Phys. Rev. B 34 (1986) 4129.
[19] O.B. Wright, K. Kawashima, Phys. Rev. Lett. 69 (1992) 1668.
[20] A. Campion, D.R. Mullins, Chem. Phys. Lett. 94 (1983) 576.
[21] R. Ryberg, Phys. Rev. B 32 (1985) 2671.
[22] P. Woodruff, T.A. Delchar, Modern Techniques of Surface Science, 2nd edn., Cambridge University Press, Cambridge, 1994, p. 532.
[23] X.D. Zhu, H. Suhr, Y.R. Shen, Phys. Rev. B 35 (1987) 3047.
[24] S. Su, P.S. Cremer, Y.R. Shen, G.A. Somorjai, Phys. Rev. Lett. 77 (1996) 3858.
[25] S. Chiang, R.G. Tobin, P.L. Richards, P.A. Thiel, Phys. Rev. Lett. 52 (1984) 648.
[26] C.J. Hirschmugl, G.P. Williams, F.M. Hoffmann, Y.J. Chabal, Phys. Rev. Lett. 65 (1990) 480.
[27] M. van Exter, Ch. Fattinger, D.R. Grischkowsky, Opt. Lett. 14 (1989) 1128.
[28] Q. Wu, X.-C. Zhang, Appl. Phys. Lett. 68 (1996) 1604.
[29] M. Hunermann, J. Geurts, W. Richter, Phys. Rev. Lett. 66 (1991) 640.
[30] N. Esser, M. Kopp, P. Haier, A. Kelnberger, W. Richter, J. Vac. Sci. Technol. B 11 (1993) 1481.
[31] G.C. Cho, W. Kutt, H. Kurz, Phys. Rev. Lett. 65 (1990) 764.
[32] W.A. Kutt, W. Albrecht, H. Kurz, IEEE J. of Quantum. Electron. 28 (1992) 2434, and references therein.
[33] M.J. Zeiger, S. Vidal, T.K. Cheng, E.P. Ippen, G. Dresselhaus, M.S. Dresselhaus, Phys. Rev. B 45 (1992) 768.
[34] T.K. Cheng, S. Vidal, M.J. Zeiger, G. Dresselhaus, M.S. Dresselhaus, E.P. Ippen, Appl. Phys. Lett. 58 (1991) 980.
[35] H.W.K. Tom, C.M. Mate, X.D. Zhu, J.E. Crowell, Y.R. Shen, G.A. Somorjai, Phys. Rev. Lett. 52 (1984) 348.

[36] T. Stehlin, M. Feller, P. Guyot-Sionnest, Y.R. Shen, Opt. Lett. 13 (1988) 389.
[37] G.O. Smith, T. Juhasz, W.E. Bron, Y.B. Levinson, Phys. Rev. Lett. 68 (1992) 2366.
[38] F. Vallée, F. Bogani, Phys. Rev. B 43 (1991) 12049.
[39] F. Vallée, Phys. Rev. B 49 (1994) 2460.
[40] F. Vallée, Solid State. Commun. 93 (1995) 741.
[41] Y.X. Yan, E.B. Gamble, K.A. Nelson, J. Chem. Phys. 83 (1985) 5391.
[42] W.E. Bron, J. Kuhl, B.K. Rhee, Phys. Rev. B 4 (1986) 6961.
[43] D. Menzel, R. Gomer, J. Chem. Phys. 41 (1964) 3311.
[44] P.A. Redhead, Can. J. Phys. 42 (1964) 886.
[45] P.R. Antoniewicz, Phys. Rev. B 21 (1980) 3811.
[46] J.A. Prybyla, T.F. Heinz, J.A. Misewich, M.M.T. Loy, J.H. Glownia, Phys. Rev. Lett. 64 (1990) 1537.
[47] J.A. Prybyla, H.W.K. Tom, G.D. Aumiller, Phys. Rev. Lett. 68 (1992) 503.
[48] F.-J. Kao, D.G. Busch, D. Cohen, D. Gomes da Costa, W. Ho, Phys. Rev. Lett. 71 (1993) 2094.
[49] J.A. Misewich, T.F. Heinz, D.M. Newns, Phys. Rev. Lett. 68 (1992) 3737.
[50] H.W.K. Tom, T.F. Heinz, Y.R. Shen, Phys. Rev. Lett. 51 (1983) 1983.
[51] J. Qi, M.S. Yeganeh, I. Koltover, A.G. Yodh, Phys. Rev. Lett. 71 (1993) 633.
[52] S.R. Armstrong, R.D. Hoare, M.E. Pemble, I.M. Povey, A. Stafford, A.G. Taylor, B.A. Joyce, J.H. Neave, J. Zhang, Surf. Sci. Lett. 291 (1993) L751.
[53] P. Drathen, W. Ranke, K. Jacobi, Surf. Sci. 77 (1978) L162.
[54] C.H. Kuo, S. Anand, R. Droopad, K.Y. Choi, G.N. Maracas, J. Vac. Sci. Technol. B 12 (1994) 1214.
[55] W.E. Bron, S. Mehta, J. Kuhl, M. Klingenstein, Phys. Rev. B 39 (1989) 12642.
[56] G.C. Cho, T. Dekorsy, H.J. Bakker, R. Hovel, H. Kurz, Phys. Rev. Lett. 77 (1996) 4062.
[57] R. Fuchs, K.L. Kliewer, Phys. Rev. 140 (1965) 2076.
[58] K. Wan, J.F. Young, Phys. Rev. B 41 (1990) 10772.
[59] A. Van Oostrum, J. Vac. Sci. Technol. 13 (1976) 224.
[60] A.U. MacRae, G.W. Gobeli, in: R.K. Willardson, A.C. Beer, Semiconductors and Semimetals, Vol. 2, Academic, New York, 1966, p. 115.
[61] L. Smit, R.M. Tromp, J.F. van der Veen, Phys. Rev. B 29 (1984) 4814.
[62] R.M. Feenstra, J.A. Stroscio, J. Tersoff, A.P. Fein, Phys. Rev. Lett. 58 (1987) 1192.
[63] P. Santini, L. Miglio, G. Benedek, U. Harten, P. Ruggerone, J.P. Toennies, Phys. Rev. B 42 (1990) 11942.
[64] P. Santini, L. Miglio, G. Benedek, U. Harten, P. Ruggerone, Surf. Sci. 241 (1991) 346.
[65] Y.R. Wang, C.B. Duke, Surf. Sci. 205 (1988) L755.
[66] T.J. Godin, J.P. LaFemina, C.B. Duke, J. Vac. Sci. Technol. B 9 (1991) 2282.
[67] P.K. Das, R.E. Allen, #1473, in: E.M. Anastassakis, J.D. Joannopoulos, Proceedings of the 20th International Conference on the Physics of Semiconductors, Thessaloniki, Greece, 1990, World Scientific, Singapore, 1990.
[68] R. Di Felice, A.I. Shkrebtii, F. Finocchi, C.M. Bertoni, G. Onida, J. Electron Spectrosc. Relat. Phenom. 64/65 (1993) 697.
[69] J. Fritsch, P. Pavone, U. Schröder, Phys. Rev. Lett. 71 (1993) 4194.
[70] R. Honke, J. Fritsch, P. Pavone, U. Schröder, Phys. Rev. B 53 (1996) 9923, The clean surface electronic structure is shown Fig. 3.
[71] U. Harten, J.P. Toennies, Europhys. Lett. 4 (1987) 833.
[72] Z.J. Gray-Grychowski, R.G. Egdell, B.A. Joyce, R.A. Stradling, K. Woodbridge, Surf. Sci. 186 (1987) 482.
[73] H. Nienhaus, W. Mönch, Phys. Rev. B 50 (1994) 11750.
[74] R.W. Bernstein, A. Borg, H. Husby, B.O. Fimland, J.K. Grepstad, Appl. Surf. Sci. 56–58 (1992) 74.
[75] A.J. Van Bommel, J.E. Crombeen, T.G.J. Van Oirschot, Surf. Sci. 72 (1978) 95.
[76] M.A. Mendez, F.J. Palomares, M.T. Cuberes, M.L. Gonzalez, F. Soria, Surf. Sci. 251/252 (1991) 145.
[77] D.K. Biegelsen, R.D. Bringans, J.E. Northrup, L.E. Swartz, Phys. Rev. B 41 (1990) 5701.
[78] J.R. Creighton, Surf. Sci. 234 (1990) 287.
[79] F.J. Palomares, M.A. Mendez, M.T. Cuberes, F. Soria, J. Vac. Sci. Technol. A 9 (1991) 939.
[80] P. Kraus, W. Nunes Rodrigues, W. Mönch, Surf. Sci. 219 (1989) 107.
[81] J.E. Northrup, S. Froyen, Phys. Rev. Lett. 71 (1993) 2276.
[82] D.J. Chadi, J. Vac. Sci. Technol. A 5 (1987) 834.
[83] M.D. Pashley, Phys. Rev. B 40 (1989) 10481.
[84] J. Cerda, F.J. Palomares, F. Soria, Phys. Rev. Lett. 75 (1995) 665.
[85] F. Stietz, J.A. Schaefer, A. Goldman, Surf. Sci. 383 (1997) 123.
[86] Q. Xue, T. Hashizume, J.M. Zhou, T. Sakata, T. Ohno, T. Sakurai, Phys. Rev. Lett. 74 (1995) 3177.
[87] K. Tone, M. Yamada, Y. Ide, Y. Katayama, Japan. J. Appl. Phys. 31 (1992) L721.
[88] L.K. Verheij, M.K. Freitag, F. Wiegershaus, Surf. Sci. 334 (1995) 105.
[89] L.K. Verheij, M.K. Freitag, F. Wiegershaus, Surf. Sci. 342 (1995) 47.
[90] L.K. Verheij, M.K. Freitag, F. Wiegershaus, Surf. Sci. 342 (1995) 55.
[91] R. Ludeke, A. Koma, J. Vac. Sci. Technol. 13 (1975) 241.
[92] J. Szuber, J. Electron Spectrosc. Relat. Phenom. 53 (1990) 19.
[93] J.M. Epp, J.G. Dillard, Chem. Mater. 2 (1990) 449.
[94] G.-P. Jiang, H.E. Ruda, J. Appl. Phys. 83 (1998) 5880.
[95] M.C.G. Passeggi Jr., I. Vaquila, J. Ferron, Appl. Surf. Sci. 133 (1998) 65.
[96] R.P. Vasquez, B.F. Lewis, F.J. Grunthaner, J. Vac. Sci. Technol. B 1 (1983) 791.
[97] G.P. Schwartz, B.V. Dutt, G.J. Gualtieri, Appl. Phys. Lett. 39 (1981) 42.
[98] N. Levinson, R. Beserman, C. Cytermann et al., Appl. Phys. Lett. 56 (1990) 1131.
[99] A. Rim, R. Beserman, J. Appl. Phys. 74 (1993) 897.
[100] G. Lupke, O. Busch, C. Meyer, H. Kurz, O. Brandt, H. Yang, A. Trampert, K.H. Ploog, G. Lucovsky, Phys. Rev. B 57 (1998) 3722.

[101] W. Daum, H.-J. Krause, U. Reichel, H. Ibach, Phys. Rev. Lett. 71 (1993) 1234.
[102] C. Meyer, G. Lupke, U. Emmerichs, F. Wolter, H. Kurz, C.H. Bjorkman, G. Lucovsky, Phys. Rev. Lett. 74 (1995) 3001.
[103] A.M. Weiner, D.E. Leaird, G.P. Weiderrecht, K.A. Nelson, Science 248 (1990) 1317.
[104] T. Dekorsky, W. Kutt, T. Pfeifer, H. Kurz, Europhys. Lett. 23 (1993) 223.
[105] S. Hunsche, K. Wienecke, T. Dekorsy, H. Kurz, Phys. Rev. Lett. 75 (1995) 1815.
[106] S. Hunsche, H. Kurz, Appl. Phys. A 65 (1997) 221.